IEEE Transactions on Automation Science and Engineering (T-ASE) paper, presented at ICRA 2026, Vienna, Austria.
Cite as T-ASE paper.

Analysis of Independent Control in Tilt-Rotor Quadrotors

Sathyanarayanan Seshasayanan, *Member, IEEE*, Sanjay Chaturvedi, and Soumya Ranjan Sahoo, *Senior Member, IEEE*

***Abstract*—The underactuation of conventional aerial vehicles limits their ability to independently control position and attitude, motivating the use of overactuated designs such as tilt-rotor quadrotors. Existing works on tilt-rotor quadrotors primarily focus on determining the minimum thrust-to-weight ratio required for hovering at arbitrary orientations. However, they do not address the maximum allowable attitude range within which independent control is feasible given specific thrust constraints. In this work, we investigate the feasible attitude range within which a tilt-rotor quadrotor can maintain independent control, given rotor thrust limits. First, we formulate the thrust constraints as convex functions and solve them using convex optimization techniques to identify feasible sets. To determine the maximum attitude that allows for independent control under thrust constraints, we pose a nonconvex optimization problem and employ a successive convex approximation (SCA) technique to compute a optimal solution, which corresponds to the optimal solution of the original nonconvex problem. Given the maximum attitude limits, we then compute the minimum thrust required per rotor to achieve independent control. Furthermore, we determine the maximum allowable disturbance magnitude that the tilt-rotor quadrotor can handle while retaining independent control. The study results are verified through processor-in-the-loop (PIL) simulations and outdoor hardware experiments on a tilt-rotor quadrotor. An illustrative video showing both the PIL simulation and hardware experimental results can be found at: `https://youtu.be/6qjc9_KtACM`**

***Note to Practitioners*—This paper is motivated by the potential application of tilt-quadrotors in inspection, search and rescue, and aerial manipulation, owing to their ability to perform agile maneuvers in confined environments. However, ensuring independent control of both position and attitude across all orientations remains a practical challenge, primarily due to limitations in rotor thrust capabilities. This work presents a practical framework to determine the range of attitudes over which independent control can be maintained, based on the available thrust from each rotor. Using convex optimization techniques, the proposed method evaluates whether the thrust capacity of the vehicle is sufficient for the desired operational envelope. If not, it also identifies the minimum thrust required per rotor to enable full-range control. Additionally, the framework assesses the maximum disturbance magnitude the system can tolerate while retaining independent control. The findings are validated through simulations and outdoor experiments on a custom-built tilt-rotor quadrotor platform, offering actionable insights for system design and mission planning.**

***Index Terms*—Convex optimization, independent control, flight maneuverability, tilt-rotor quadrotor.**

Received 24 April 2025; revised 15 September 2025 and 10 November 2025; accepted 9 December 2025. Date of publication 15 December 2025; date of current version 12 January 2026. This article was recommended for publication by Associate Editor R. Carli and Editor M. Dotoli upon evaluation of the reviewers' comments. *(Corresponding author: Sathyanarayanan Seshasayanan.)*

Sathyanarayanan Seshasayanan is with the Department of Computer Science, Electrical and Space Engineering, Luleå University of Technology, 971 87 Luleå, Sweden (e-mail: satses@associated.ltu.se).

Sanjay Chaturvedi and Soumya Ranjan Sahoo are with the Electrical Engineering Department, Indian Institute of Technology Kanpur, Kanpur 208016, India (e-mail: sanjayc@iitk.ac.in; srsahoo@iitk.ac.in).

Digital Object Identifier 10.1109/TASE.2025.3644498

I. Introduction

THE vertical takeoff and landing (VTOL) capability, high maneuverability, and simple mechanical design have established rotary-wing uncrewed aerial vehicles (UAVs) as one of the most widely used UAV platforms [1]. These UAVs are employed across various fields for multiple applications. They are used for remote inspection of pipelines, industries with confined spaces, and elevated installations such as distillation columns and transmission lines [2]. Deploying UAVs for search and rescue operations in constrained and unknown urban environments has become the new normal [3]. Additionally, they are utilized in 3D modeling of historical sites [4], load transport [5], [6], visual based target tracking [7], [8], and studies of pest-borne diseases [9]. UAVs equipped with robotic arms have demonstrated potential in centimeter-level aerial assembly [10].

Most of these applications utilize quadrotors with fixed rotors generating unidirectional thrust. However, this unidirectional thrust makes the UAVs underactuated [11], and does not allow independent control of attitude and position. As a result, a quadrotor cannot maintain its position while changing its attitude, requiring it to land multiple times in tasks such as search and rescue operations in constrained environments [3]. Furthermore, conventional quadrotors face challenges in applications that require physical interaction with the environment, such as autonomous door opening [12] and contact-based inspections [13], [14]. These aerial robotic manipulators must interact physically with the environment, necessitating the decoupled control of quadrotors' attitude and position. As conventional quadrotors with fixed rotors are underactuated platforms that do not allow independent control of position and attitude, we now move towards finding a solution to this problem. In [15], various multirotor designs are reviewed and classified based on under, fully or over-actuated UAVs. One such overactuated UAV is the omnicopters, which have unidirectional thrust rotors fixed to the body at tilted angles [11]. However, a major drawback of this design is the reduced system efficiency and overall flight duration due to the counteracting forces inherent in this configuration. In [16], a fault tolerance controller is designed for an overactuated UAV platform composed of quadcopters mounted on passive joints

IEEE Transactions on Automation Science and Engineering (T-ASE) paper, presented at ICRA 2026, Vienna, Austria.

is proposed. The another overactuated UAV is the tilt-rotor quadrotors, where all four unidirectional rotors can tilt about an axis passing through the quadrotor arm to which the rotor unit is attached [17].

Works done by [17] and [18] were the first attempts to present a study on tilt-rotor quadrotors, whereas later on, the work done in [19] presented the actual flight test results of such a quadrotor. The work of tilt-rotor quadrotor control and modelling is then carried forward in the works of many researchers, which includes the work done in [20], [21], [22], [23], [24], and [25], to name a few.

Ryll et al., in their work [19], presented the quadrotor prototype for a tilt-rotor quadrotor with an emphasis on hardware and software specifications to conduct the first flight of such a prototype. In their later work, they designed an optimal control scheme that minimised total inflight energy consumption and demonstrated the independent control ability of these quadrotors through flight tests [20]. Invernizzi et al., in their paper, proposed a thrust-vector-based control approach for a quadrotor with tiltable rotors [21], incorporating limits on rotor tilt angles when designing their position-tracking controller. Later, in [24], they compared the performance of a quasi-time-optimal control scheme with existing feedback linearization-based controllers for a tilt-rotor quadrotor. In [22], Bhargavapuri et al. presented a controller for a tilt-rotor quadrotor with a bound on the tilt angle of rotors. They used a control allocation assuming small tilt angles. Later, in [26], they demonstrated autonomous tracking and landing of their fully-actuated quadrotor. In [27], an optimal geometric control allocation strategy was proposed for a biaxial-tilt quadrotor (Quad3DV). In [25], the authors propose a dual-level adaptive controller with optimal control allocation for an H-configuration tilt-rotor quadrotor.

All these works have presented the design of such types of quadrotors, their controller design, and the control allocation. However, these works need a discussion on finding the attitude range for a given tilt-rotor quadrotor within which the independent control of the position and the attitude is feasible. Nemati et al. [28] have designed a controller that can achieve independent controller at any value of pitch or roll angle; similarly, work done by Oosedo et al. in [23] presented an attitude controller that enables attitude transitions for pitch angles ranging 0 to 90 degrees. Nevertheless, even in these works, we have not found any discussion on finding the range of attitudes for the tilt-rotor quadrotor used within which it will have decoupled control of position and attitude. In [29], the authors discuss the degree of coupling between the total force and total moment generated by the rotors for various tilt-rotor multirotors. However, this degree of coupling is considered without any constraint on actuator limit. Several studies have investigated control and actuation limits in tilt-rotor multirotors. In [30], the static hovering capability of tilt-rotor trirotors is analyzed, and the minimum per-rotor thrust for hovering at different orientations is computed, but the feasible attitude range for independent control is not addressed. In [31], the focus is on optimal rotor placement to maximize force generation for tilt-rotor multirotors. While this improves the system's force capability, the study does not consider the attitude range feasibility of independent control. Similarly, [32] presents a real-time method for generating feasible reference trajectories for a bi-axial tilt-rotor quadrotor under actuator constraints. While the approach ensures feasibility of a reference trajectory from a given set, it does not characterize the full attitude range over which independent control is possible, nor does it provide analytical tools for evaluating attitude feasibility bounds based on actuator limitations.

Existing works [30], [31], [32] primarily focus on static hovering analysis or trajectory feasibility, without addressing the maximum feasible attitude range for independent control under rotor thrust constraints in overactuated UAVs. The present work fills this gap by presenting a systematic method to explicitly compute the maximum attitude range that guarantees independent control, using convex optimization and successive convex approximation (SCA) techniques, given actuator limitations.

A. Paper Contributions

While existing References show that considerable work has been done in the design and development of tilt-rotor multirotors with various controllers, it is clear that a study is needed to estimate the feasible range of attitudes for independent control, given the thrust generated by each rotor, in a tilt-rotor quadrotor. This analysis will help in planning the missions for a given tilt-rotor quadrotor by knowing the attitude range within which the position and attitude control are decoupled. Additionally, it will assist in selecting a suitable rotor unit for a tilt-rotor quadrotor based on specific application requirements.

The significant contributions of this work is as follows:

1) We determine the feasible attitude set (defined by pitch and roll angles) within which the tilt-rotor quadrotor can independently control its position and orientation, given constraints on rotor thrust. To the best of the authors knowledge, this has not been addressed prior.
2) To precisely compute the boundary points of this feasible set, we formulate a constrained optimization problem with nonconvex constraints and solve it using a SCA.
3) We prove that the solution obtained via the SCA method corresponds to a locally optimal solution of the original nonconvex optimization problem.
4) By analyzing the extreme points of the feasible attitude set, we derive the minimum required thrust per rotor to guarantee independent control across the full attitude range. This is distinct from prior work such as [30], which only determines the minimum thrust-to-weight ratio for maintaining static hovering at arbitrary orientations without enabling motion or torque in all directions.
5) Finally, we quantify the maximum external disturbance that the tilt-rotor quadrotor can tolerate while still maintaining its ability for independent control of position and orientation.

The remaining paper are organised as follows: Section II discuss the mathematical model of tilt-rotor quadrotor. Section III presents the feasible set of attitude, minimum thrust required and effect of disturbance on the feasible set for which tilt-rotor quadrotor can independently control its position and

IEEE Transactions on Automation Science and Engineering (T-ASE) paper, presented at ICRA 2026, Vienna, Austria.

orientation. Section IV validates the above results through PIL simulations. Section V discusses the maneuverability of the in-house developed tilt quadrotor. Finally, Section VI provides the conclusions of this study.

B. Abbreviations and Acronyms

Throughout this paper, $\mathcal{F}_B$ and $\mathcal{F}_I$ denote body frame and inertial frame, respectively. $\mathcal{I}_n$ denotes n-dimentional identity matrix. $\Re^n$ denotes the n-dimensional Euclidean spaces and the notation $\Re^{m\times n}$ denotes space of real matrices of size $m\times n$. $\mathcal{M}^\top$ represents the transpose of the matrix $\mathcal{M}$. $(i,j)^{th}$ element in the matrix $\mathcal{M}$ is represented as $\mathcal{M}_{i,j}$. The set of positive real numbers are denoted as $\Re^+ := \{x \in \Re | x > 0\}$. The absolute value or the magnitude of $x \in \Re$ is denoted as $|x|$. For $x \in \Re$, non zero-sign function is represented as sign(.), which is given by, $\text{sign}(x) = \begin{cases} 1, & \text{if } x \geq 0 \\ -1, & \text{otherwise} \end{cases}$ The four-quadrant inverse tangent is represented as atan2(.). rank($\mathcal{M}$) is the rank of the matrix $\mathcal{M}$. det($\mathcal{M}$) is the determinant of the matrix $\mathcal{M}$. $\times$ represents the cross product of two vectors. The set $SO(3) := \{\mathbf{R} \in \Re^{3\times3} : \mathbf{R}^\top\mathbf{R} = \mathcal{I}_3, det(\mathbf{R}) = 1\}$. $\|\mathbf{d}\|_\infty := \max_i\{|d_i|\}, \forall i = \{1,2,3..n\}$ is the l_∞ norm of the vector $\mathbf{d} \in \Re^n$. $\mathcal{M} \geq 0$ denotes that the matrix $\mathcal{M} \in \Re^{n\times n}$ is a positive semidefinite. The trigonometry functions are represented as $\sin \triangleq s$, $\cos \triangleq c$.

II. Mathematical Modeling

This section discusses the dynamic model of a +- configure tilt-rotor quadrotor. The following assumptions are made in line with [19], [33] while developing this model:

Assumption 1: The vehicle is rigid and symmetric about the body axis.

Assumption 2: Thrust and drag moment produced by a rotor is directly proportional to the square of the angular speed of the rotor.

Assumption 3: The vehicle's center-of-gravity (COG) coincides with the origin of the body frame.

In this paper, NED (X_I-north and Y_I-east and Z_I-down) convention is chosen, which acts as an inertial frame of reference $\mathcal{F}_I : \{O_I; X_I, Y_I, Z_I\}$. Let $\mathcal{F}_B : \{O_B; X_B, Y_B, Z_B\}$ be the body frame which is attached on tilt-rotor quadrotor. As per Assumption 2, the thrusts F_i and drag moments M_i generated by i^{th} rotor can be written as,

$$\begin{aligned} F_i &= k_f\omega_i^2, \\ M_i &= k_m\omega_i^2, \end{aligned} \tag{1}$$

where ω_i is the angular speed of i^{th} rotor, k_f and k_m are the force and drag moment constants, respectively. The orientation of vehicle frame $\mathcal{F}_B$ with respect to inertial frame $\mathcal{F}_I$ is represented in terms of rotation matrix ${}^I\mathbf{R}_B \in SO(3)$ as,

$${}^I\mathbf{R}_B = \begin{bmatrix} c_\theta c_\psi & c_\psi s_\phi s_\theta - c_\phi s_\psi & s_\phi s_\psi + c_\phi c_\psi s_\theta \\ c_\theta s_\psi & c_\phi c_\psi + s_\phi s_\theta s_\psi & c_\phi s_\theta s_\psi - c_\psi s_\phi \\ -s_\theta & c_\theta s_\phi & c_\phi c_\theta \end{bmatrix}, \tag{2}$$

where ϕ, θ, ψ represent the roll, pitch and yaw angles of Eulers' ZYX sequence. The model of the tilt-rotor quadrotor using Newton-Euler equations under the Assumptions 2-3 is as follows, [19],

$$\begin{bmatrix} \ddot{\mathbf{p}} \\ \mathcal{J}\dot{\mathbf{\Omega}} \end{bmatrix} = \begin{bmatrix} {}^I\mathbf{R}_B\dfrac{\mathbf{F}_B}{m} + \mathbf{G} + {}^I\mathbf{R}_B\mathbf{d}_f + \mathbf{F}_d \\ (\mathcal{J}\mathbf{\Omega}) \times \mathbf{\Omega} + \mathbf{M}_B + \mathbf{d}_m + \mathbf{M}_{gyro} \end{bmatrix}, \tag{3}$$

where $\mathbf{G} = [0,0,g]^\top$, $\mathbf{p} = [x,y,z]^\top \in \Re^3$ is the position vector of O_B in $\mathcal{F}_I$, $\mathbf{\Omega} := [\Omega_1, \Omega_2, \Omega_3]^\top \in \Re^3$ is the angular velocity in $\mathcal{F}_B$, g is acceleration due to gravity in the Z direction, $\mathcal{J} \in \Re^{3\times3}$ is the inertia matrix in $\mathcal{F}_B$ and m is mass of the vehicle. The force and torque disturbances caused by wind are denoted by $\mathbf{d}_f \in \mathbb{R}^3$ and $\mathbf{d}_m \in \mathbb{R}^3$, respectively, and are expressed in the body-fixed frame $\mathcal{F}_B$. The aerodynamic drag force and the gyroscopic torque resulting from the spinning of the rotors are denoted by $\mathbf{F}_d$ and $\mathbf{M}$gyro, respectively. The control torque $\mathbf{M}_B \in \Re^3$ and the control force $\mathbf{F}_B \in \Re^3$ are defined in body frame $\mathcal{F}_B$. The thrust F_i and moments M_i due to i^{th} rotor are resolved along the body frame, thus leading to nonlinear expressions in tilt angles (α_i). The drag force [34] is expressed as

$$\mathbf{F}_d = -D_b\mathbf{v}_b, \tag{4}$$

where $\mathbf{v}_b$ is the vehicle velocity in $\mathcal{F}_B$-frame and D_b is drag coefficient. There are other aerodynamic forces, such as blade flapping and airflow disruptions, which have significant effects only at high velocities [35]. In this work, we focus on whether the vehicle can move at low speeds while maintaining various attitudes. Therefore, we have neglected these terms in the model. The gyroscopic torque due to spinning of rotors is given by

$$\begin{aligned} \mathbf{M}_{gyro} = &\sum_{i=1}^{4} I_r\omega_i c_{\alpha_i}(\mathbf{\Omega} \times Z_B) \\ &+ \sum_{j=1}^{2} I_r\omega_{2j-1}s_{\alpha_{2j-1}}(\mathbf{\Omega} \times Y_B) \\ &+ \sum_{j=1}^{2} I_r\omega_{2j}s_{\alpha_{2j}}(\mathbf{\Omega} \times X_B) \end{aligned} \tag{5}$$

where I_r is the moment of inertia of rotors. The positive measurement for tilt angles α_1 and α_3 is along the X_B-axis, whereas for α_2 and α_4 is along the Y_B-axis. Thus, control torque and force are given by,

$$\begin{bmatrix} M_{b1} \\ M_{b2} \\ M_{b3} \end{bmatrix} = \begin{bmatrix} l\left(-F_1c_{\alpha_1} + F_2c_{\alpha_2}\right) + M_1s_{\alpha_1} + M_2s_{\alpha_2} \\ l\left(F_3c_{\alpha_3} - F_4c_{\alpha_4}\right) + M_3s_{\alpha_3} + M_4s_{\alpha_4} \\ m_1 - m_2 \end{bmatrix} \tag{6}$$

$$\begin{bmatrix} F_{b1} \\ F_{b2} \\ F_{b3} \end{bmatrix} = \begin{bmatrix} -F_1s_{\alpha_1} - F_2s_{\alpha_2} \\ F_3s_{\alpha_3} + F_4s_{\alpha_4} \\ -F_1c_{\alpha_1} - F_2c_{\alpha_2} - F_3c_{\alpha_3} - F_4c_{\alpha_4} \end{bmatrix}, \tag{7}$$

where $m_1 = l\left(F_1s_{\alpha_1} - F_2s_{\alpha_2} + F_3s_{\alpha_3} - F_4s_{\alpha_4}\right)$, $m_2 = M_1c_{\alpha_1} + M_2c_{\alpha_2} - M_3c_{\alpha_3} - M_4c_{\alpha_4}$ and l is the distance between COG of the tilt-rotor quadrotor and its each rotor. Given the system dynamics, the feasible set of attitude angles for which tilt-rotor quadrotor can independently control its position and orientation is discussed in the next section.

Remark 1: For a conventional quadrotor, the rotor tilt angles are fixed at 0, implying that all thrust vectors are aligned with

IEEE Transactions on Automation Science and Engineering (T-ASE) paper, presented at ICRA 2026, Vienna, Austria.

the body z-axis. As a result, the components of the net force along the body x- and y-axes become zero in (7), indicating that the vehicle cannot generate force in these directions. Therefore, a conventional quadrotor is underactuated.

III. Independent Control of Position and Attitude

Conventional quadrotors are underactuated systems since they have only four inputs for six degrees of freedom. Even conventional hexarotors and octorotors are underactuated due to mechanical constraints, despite having more inputs than degrees of freedom. Thus, decoupling of attitude and position cannot be achieved in these vehicles.

To prove that the tilt-rotor quadrotor can decouple position and attitude control, it must be able to independently generate force and torque in any direction. Let $\mathcal{M}$ denote the mapping between the thrust generated by each rotor and the resulting force and torque acting on the vehicle. For independent generation of force and torque in all directions, $\mathcal{M}$ must have full rank [33].

Due to rotor tilting, the thrust generated by each rotor decomposes into two components, one perpendicular to the plane of the vehicle and one parallel to the plane. Let $\mathbf{f}$ be the vector of dimension 8×1 containing the perpendicular thrusts $f_{v,i} := F_i\, c_{\alpha_i}$ and the horizontal thrusts $f_{h,i} := F_i\, s_{\alpha_i}, \forall i \in \{1,2,3,4\}$, such that,

$$\mathbf{f} = \left[f_{h,1}, f_{v,1}, f_{h,2}, f_{v,2}, f_{h,3}, f_{v,3}, f_{h,4}, f_{v,4}\right]^\top. \tag{8}$$

Using (1), from (6) and (7), $\mathbf{F}_B$ and $\mathbf{M}_B$ can be expressed in a linear relation to $\mathbf{f}$ as

$$\begin{bmatrix}\mathbf{F}_B \\ \mathbf{M}_B\end{bmatrix} = \mathcal{M}\mathbf{f}, \tag{9}$$

where $\mathcal{M}$ is a matrix of dimension 6×8 given by,

$$\mathcal{M} = \begin{bmatrix} -1 & 0 & -1 & 0 & 0 & 0 & 0 & 0 \\ 0 & 0 & 0 & 0 & 1 & 0 & 1 & 0 \\ 0 & -1 & 0 & -1 & 0 & -1 & 0 & -1 \\ \frac{k_m}{k_f} & -l & \frac{k_m}{k_f} & l & 0 & 0 & 0 & 0 \\ 0 & 0 & 0 & 0 & \frac{k_m}{k_f} & l & \frac{k_m}{k_f} & -l \\ l & \frac{k_m}{k_f} & -l & \frac{k_m}{k_f} & l & -\frac{k_m}{k_f} & -l & -\frac{k_m}{k_f} \end{bmatrix}. \tag{10}$$

Here, $\mathcal{M}$ has full row rank since the determinant of the matrix $\mathcal{M}\mathcal{M}^\top$ is $256l^4\left(\frac{k_m^2}{k_f^2} + l^2\right) \neq 0$. Thus, from (9), the vehicle can generate force and torque in any direction without constraints on thrusts (F_i) or tilt angles (α_i). While the tilt-angles are in the full angular range $[-\pi, \pi]$, the thrusts (F_i) are upper-bounded, typically depending on the motor-propeller combination.

The following subsections discuss the feasible orientations in which the vehicle can generate force and torque in any direction given the constraint on F_i. All optimization problems in this paper are solved using `MATLAB` with the `cvx` interface [36], [37], which uses a semi-definite programming (SDP) algorithm.

TABLE I
Parameters Used in Mathematical Model

Parameters	Value
Acceleration due to gravity g	9.8 m/sec^2
Air density ρ	1.225 kg/m
Maximum Area of the vehicle A	0.16 m^2
Mass of tilt-rotor quadrotor m	2.1kg
Length of the arm d	0.22m
Maximum vehicle velocity	12 m/sec
Drag coefficient D_b	0.02 kg/sec
Maximum Rotor speed ω_i	1200 rad/s
Maximum angular velocity of vehicle Ω_i	2 rad/sec
Moment of inertia of the rotor I_r	13×10^{-6} kg/m
Aerodynamic Drag coefficient C_d	0.2
Ratio of drag by force constant $\frac{k_m}{k_f}$	0.038

A. Feasible Set S

Similar to a conventional quadrotor, in a tilt-rotor quadrotor each rotor is typically designed to provide a maximum thrust equal to half of the vehicle's weight [38]. This constraint can be expressed as

$$F_i \leq \frac{m\,g}{2}, \quad \forall i \in \{1,2,3,4\}. \tag{11}$$

For hovering, the total thrust generated by rotors along the inertial frame Z-axis should be equal to the mg. This weight expressed in $\mathcal{F}_B$-frame ($\mathbf{W}_B \in \Re^3$), depends on the ϕ and θ as given in (12). Thus, the objective is to find the feasible set S consisting of roll (ϕ) and pitch (θ) angles that satisfy the (11) and can generate force and torque in all directions in the set S.

$$\mathbf{W}_B(\phi,\theta) = \begin{bmatrix} W_{b1}(\phi,\theta) \\ W_{b2}(\phi,\theta) \\ W_{b3}(\phi,\theta) \end{bmatrix} = m\,{}^B\mathbf{R}_I \begin{bmatrix} 0 \\ 0 \\ g \end{bmatrix} = \begin{bmatrix} -m\,g s_\theta \\ m\,g c_\theta s_\phi \\ m\,g c_\theta c_\phi \end{bmatrix}. \tag{12}$$

For simplicity, let's first assume that there are no disturbances. Due to constraint in (11) and using (9) and (12), the vehicle is unable to generate any additional force along the body x-axis when $\theta = \pm 90°$. Consequently, at this extreme attitude, the vehicle cannot independently control both its position and orientation. Therefore, it is necessary to determine the maximum attitude range within which the vehicle can maintain independent control of its position and orientation.

For given attitude, the vehicle should be able to balance its own weight and also be able to generate additional force and moment in all directions for maneuverability. These additional forces and moments must also compensate for the drag forces $\mathbf{F}_d$ and gyroscopic moments $\mathbf{M}_{gyro}$. From Table I, the maximum value magnitude of $\mathbf{F}_d := [F_{d,1}, F_{d,2}, F_{d,3}]^\top$ and $\mathbf{M}_{gyro} := [M_{g,1}, M_{g,2}, M_{g,3}]^\top$ are found to be

$$\begin{aligned} |F_{d,i}| \leq |F_d| \approx 0.24\ N, \quad \forall i \in \{1,2,3\} \\ |M_{g,i}| \leq |M_g| \approx 0.2162\ Nm, \quad \forall i \in \{1,2,3\} \end{aligned} \tag{13}$$

Thus, the additional force and moment in all direction are denoted as ϵ, and γ, respectively, such that $|F_d| < \epsilon \in \Re^+$, and $|M_g| < \gamma \in \Re^+$. For independent control, the vehicle must be capable of balancing its own weight while simultaneously generating these additional forces and moments in all

IEEE Transactions on Automation Science and Engineering (T-ASE) paper, presented at ICRA 2026, Vienna, Austria.

directions. This requirement can be mathematically expressed as:

$$\begin{aligned} -\epsilon \le F_{bj} + W_{bj}(\phi,\theta) \le \epsilon, \\ -\gamma \le M_{bj} \le \gamma, \quad \forall j \in \{1,2,3\}. \end{aligned} \tag{14}$$

From (8), given $\mathbf{f}$, thrust F_i and rotor orientation α_i can be calculated $\forall i \in \{1,2,3,4\}$ as,

$$F_i = \sqrt{f_{v,i}^2 + f_{h,i}^2}, \ \alpha_i = \text{atan2}(f_{v,i}, f_{h,i}). \tag{15}$$

Using (11) and (15), the constraints on rotor thrust are

$$\| \left[f_{h,i}, f_{v,i}\right]^T \|_2 \le \frac{m\,g}{2}, \quad \forall i \in \{1,2,3,4\}. \tag{16}$$

From (14), F_{bj}, M_{bj} can take two extreme values,

$$F_{bj} = -W_{bj}(\phi,\theta) \pm \epsilon, \quad M_{bj} = \pm\gamma, \quad \forall j \in \{1,2,3\}. \tag{17}$$

From (17), the total number of distinct combinations of F_{bj}, M_{bj} are $2^3 \times 2^3 = 8 \times 8 = 64$. Since the constraints (9) and (16) are linear and convex, if they are satisfied for all 64 distinct combination of F_{bj}, M_{bj} given in (17), then the interior values of F_{bj}, M_{bj} in (14) will also satisfy these constraints, as interior values can be expressed as convex combinations of the 64 distinct combinations given in (17) [39]. Thus, it is required to check whether the constraints in (9) and (16) are satisfied at the extreme values of F_{bj}, M_{bj} given in (17). From (17), there are 8 different combination points for $\mathbf{M}_B$, which are given below,

$$\begin{aligned} \mathbf{N}_1(\gamma) &= [\ \gamma, -\gamma, -\gamma]^\top, \quad \mathbf{N}_2(\gamma) = [\ \gamma, \ \gamma, -\gamma]^\top, \\ \mathbf{N}_3(\gamma) &= [-\gamma, -\gamma, -\gamma]^\top, \quad \mathbf{N}_4(\gamma) = [-\gamma, \ \gamma, -\gamma]^\top, \\ \mathbf{N}_5(\gamma) &= [-\gamma, \ \gamma, \ \gamma]^\top, \quad \mathbf{N}_6(\gamma) = [-\gamma, -\gamma, \ \gamma]^\top, \\ \mathbf{N}_7(\gamma) &= [\ \gamma, \ \gamma, \ \gamma]^\top, \quad \mathbf{N}_8(\gamma) = [\ \gamma, -\gamma, \ \gamma]^\top, \end{aligned} \tag{18}$$

The maximum value of $|F_{bj}|$ occurs when additional force of ϵ is of the same sign as W_{bj}. So, we consider the $\mathbf{F}_B$ to be:

$$F_{bj} = -W_{bj} - \epsilon \text{sign}(W_{bj}), \quad \forall j \in \{1,2,3\}. \tag{19}$$

Using (18) and (19), let $\mathbf{u} \in \Re^6$ be defined as:

$$\mathbf{u}(\phi,\theta,\epsilon,\gamma,\mathbf{N}_j) = \begin{bmatrix} F_{b1} \\ F_{b2} \\ F_{b3} \\ \mathbf{M}_B \end{bmatrix} = \begin{bmatrix} -W_{b1} - \epsilon\text{sign}(W_{b1}) \\ -W_{b2} - \epsilon\text{sign}(W_{b2}) \\ -W_{b3} - \epsilon\text{sign}(W_{b3}) \\ \mathbf{N}_j(\gamma) \end{bmatrix}. \tag{20}$$

Using (9), (10), (20), the relation between $\mathbf{f}$ and $\mathbf{u}$ is written as,

$$\mathcal{M}\mathbf{f} = \mathbf{u}(\phi,\theta,\epsilon,\gamma,\mathbf{N}_j), \quad \forall j \in \{1,\ldots,8\}. \tag{21}$$

Consider the following points of $[\phi,\theta] \in \left[-\frac{\pi}{2}, \frac{\pi}{2}\right]$, defined by

$$r_1 : (\phi,\theta), \ r_2 : (-\phi,\theta), \ r_3 : (\phi,-\theta), \ r_4 : (-\phi,-\theta) \tag{22}$$

Next, we show that if all the points defined in (22) satisfy (16) and (21) for the $\mathbf{u}$ defined in (20), then it follows that the pair $[\phi,\theta]$ satisfies all distinct 64 combination of F_{bj}, M_{bj} defined in (17). Consequently, $[\phi,\theta]$ belongs to the feasible set S and $[n\pi \pm \phi, n\pi \pm \theta]$, for any $n \in \mathbb{N}$, also belong to the feasible set S.

Lemma 1: If all the pairs of $[\phi,\theta] \in \left[-\frac{\pi}{2}, \frac{\pi}{2}\right]$ given in (22), satisfy the constraints in (16) and (21) for the $\mathbf{u}$ defined in (20), then these pairs of $[\phi,\theta]$ belongs to the feasible set S. Moreover, all points of the form $[n\pi \pm \phi, n\pi \pm \theta]$, for any $n \in \mathbb{N}$, also belong to the feasible set S.

Proof: The goal is to show that if the four roll–pitch configurations in (22) satisfy the feasibility constraints (given in (16) and (21)) for the $\mathbf{u}$ defined in (20), then all interior points defined in (14) are also feasible. This is achieved by using the convexity of the constraints and their symmetry about the origin in $\mathbf{f}$.

The feasible set S consists of all $[\phi,\theta]$ pairs that satisfy the constraints (9) and (16). These constraints are convex in $\mathbf{f}$. Therefore, if feasibility is ensured at all extreme points of $\mathbf{F}_b$ and $\mathbf{M}_b$ defined in (17), then the feasibility at all interior points automatically follows from convexity.

From (17), there are 64 distinct combinations of force and moment pairs. However, the constraint in (16) is symmetric about the origin, implying that if $\left[f_{h,i}, f_{v,i}\right]$ satisfies it, then $\left[-f_{h,i}, -f_{v,i}\right]$ will also satisfies it. Thus, by the equality constraint (9), if $[\mathbf{F}_b, \mathbf{M}_b]$ is feasible, then $[-\mathbf{F}_b, -\mathbf{M}_b]$ is also feasible.

Therefore, only 32 distinct points need to be verified. These correspond to 4 roll–pitch configurations defined in (22), each associated with 8 different moment combinations given in (18). Verifying these 32 points are sufficient to ensure that all 64 extreme combinations, and consequently the entire set defined in (14), are satisfied. Next, we establish the relationship between these 32 points and the 64 extreme points defined in (17), and demonstrate that satisfying the feasibility conditions for these 32 points automatically guarantees feasibility for the remaining 32 symmetric counterparts.

Using (12) and (19), the force components F_{bj} corresponding to the configurations in (22) attain the following combinations:

$$\begin{aligned} r_1 : \mathbf{F}_b &= [\ T_1, -T_2, -T_3]^\top, \quad r_2 : \mathbf{F}_b = [\ T_1, \ T_2, -T_3]^\top, \\ r_3 : \mathbf{F}_b &= [-T_1, -T_2, -T_3]^\top, \quad r_4 : \mathbf{F}_b = [-T_1, \ T_2, -T_3]^\top, \end{aligned} \tag{23}$$

where $T_j = |W_{bj}(\phi,\theta)| + \epsilon$, for all $j \in \{1,2,3\}$.

If $\mathbf{u}$ satisfies (16) and (21), then so does $-\mathbf{u}$. Moreover, since $-\mathbf{N}_j = \mathbf{N}_{j+4}$, for $j \in \{1,2,3,4\}$, thus, if (23) satisfies (16) and (21) for all values of $\mathbf{N}_j$, then $-\mathbf{F}_b$ also satisfies these constraints for all values of $\mathbf{N}_j$.

All the force vectors in (23), along with their negatives, satisfy all extreme values of F_{bj} given in (17). Therefore, if the 4 roll–pitch pairs $[\phi,\theta]$ given in (22) satisfy (16) and (21), then all 64 combinations of F_{bj}, M_{bj} in (17) are also satisfied. Hence, $[\phi,\theta]$ belongs to the feasible set S.

Finally, since $T_j = |W_{bj}(\phi,\theta)| + \epsilon$ depends on the absolute value of W_{bj}, and $W_{bj}(\phi,\theta)$ is periodic in both ϕ and θ, it follows that $[n\pi \pm \phi, n\pi \pm \theta] \in S$, for any $n \in \mathbb{N}$. □

With $\epsilon = \gamma = 1$ and the parameters given in Table I, objective is to look for the values of θ and ϕ that satisfy the constraints (16) and (21). For each value of ϕ and θ within the range $\left[\frac{-\pi}{2}, \frac{\pi}{2}\right]$, we use the `cvx` interface to determine whether the constraints (16), and (21) are satisfied. Let this

IEEE Transactions on Automation Science and Engineering (T-ASE) paper, presented at ICRA 2026, Vienna, Austria.

Algorithm 1 Computation of Boundary Points of the Feasible Set

Initialize step size $q \leftarrow \pi/180$, counters $i \leftarrow 0$, and $\phi, \theta \in [-\pi/2, \pi/2]$
for $v = -\pi/2 : q : \pi/2$ **do**
  for $w = -\pi/2 : q : \pi/2$ **do**
    Set $\phi \leftarrow v$, $\theta \leftarrow w$
    if constraints (16), (21) are violated **then**
      $i \leftarrow i + 1$
      Store nearest feasible boundary point:

$$(\phi^*[i], \theta^*[i]) = \begin{cases} (\phi, \theta - q), & w > -\pi/2, \\ (\phi - q, \theta), & v > -\pi/2. \end{cases}$$

      break
    end if
  end for
end for
return $[\phi^*, \theta^*]$

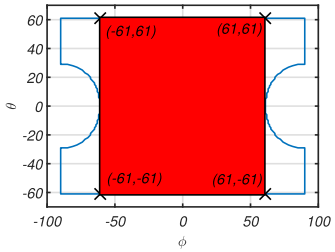

Fig. 1. Region within the blue curve for which tilt-rotor quadrotor can have independent control in all directions. ϕ and θ are independent of each other in red shaded region.

set be denoted as S_1 where each value of ϕ and θ satisfy the constraints (16), and (21).

The Algorithm 1 identifies the boundary points of the feasible set S_1 for $\phi, \theta \in \left[-\frac{\pi}{2}, \frac{\pi}{2}\right]$. It performs a grid search over the domain with a step size $q = \frac{\pi}{180}$ (1° increments). For each fixed ϕ, it sweeps through θ values from $-\frac{\pi}{2}$ to $\frac{\pi}{2}$. If a constraint violation is detected at a given (ϕ, θ), the last feasible point just before the violation ($\theta - q$ or $\phi - q$) is recorded as a boundary point. The search then moves to the next value of ϕ, repeating the process until the entire domain is scanned. Finally, the set of all such recorded pairs $(\phi^*[i], \theta^*[i])$ constitutes an approximation of the boundary of the feasible set S_1. Figure 1 shows the ranges of ϕ and θ that satisfy the constraints. From the figure it is observed that the boundary of the feasible set S_1 are symmetric with respect to the $\phi = 0$ and $\theta = 0$ axes. For each point (ϕ, θ) inside this blue curve, there exist corresponding pairs of (ϕ, θ) given in (22) which also lie inside the blue curve. Thus, the region within the blue curves in Fig. 1 shows the ranges of ϕ and θ for which the tilt-rotor quadrotor can independently control force and torque in all directions. The red shaded region denotes the maximum area where pitch (θ) and roll (ϕ) are independent of each other.

To determine the exact boundary of this red shaded region, we compute the maximum feasible pitch angle θ that satisfies the constraints given in (11) and (21), under the condition $|\phi| = |\theta|$. This leads to the following constrained optimization problem:

$$\begin{aligned} &\underset{\mathbf{f},\theta,\phi}{\text{minimize}} \quad -\theta \\ &\text{subject to: (16), (21), and, } \theta \le \frac{\pi}{2}. \end{aligned} \tag{24}$$

The constraint ((21)) in (24) is nonlinear and nonconvex due to its trigonometric dependency on (ϕ, θ). To address this, we employ a SCA technique. At each iteration k, the nonlinear equality constraint is approximated by a first-order Taylor expansion around the current estimates $\mathbf{f}_k, \theta_k$, leading to the following convex optimization problem:

$$\begin{aligned} \underset{\mathbf{f},\theta,\phi}{\text{minimize}} \quad & -\theta \\ \text{subject to:} \quad & \mathcal{M}\mathbf{f} = {}^q\hat{\mathbf{u}}(\theta, \epsilon, \gamma, \mathbf{N}_j), \\ & \|[f_{v,i}, f_{h,i}]\|_2^2 \le \frac{m^2 g^2}{4}, \quad \forall i \in \{1,2,3,4\}, \\ & \theta_k \le \frac{\pi}{2}, \end{aligned} \tag{25}$$

where

$${}^q\hat{\mathbf{u}}(\theta, \epsilon, \gamma, \mathbf{N}_j) = \mathbf{v}_q(\theta_k, \epsilon, \gamma, \mathbf{N}_j) + \left.\frac{\partial \mathbf{v}_q}{\partial \theta}\right|_{\theta=\theta_k} (\theta - \theta_k), \quad q \in \{1,2,3,4\}. \tag{26}$$

and the values of $\mathbf{v}_q$ for various points defined in (22) with $\phi = \theta$ are

$$\begin{aligned} &\mathbf{v}_1 = \mathbf{u}(\theta, \theta, \epsilon, \gamma, \mathbf{N}_j), \quad \mathbf{v}_2 = \mathbf{u}(-\theta, \theta, \epsilon, \gamma, \mathbf{N}_j), \\ &\mathbf{v}_3 = \mathbf{u}(\theta, -\theta, \epsilon, \gamma, \mathbf{N}_j), \quad \mathbf{v}_4 = \mathbf{u}(-\theta, -\theta, \epsilon, \gamma, \mathbf{N}_j), \end{aligned} \tag{27}$$

Let $\mathbf{f}^*$ and θ^* denote the optimal solution of (25). We update:

$$\mathbf{f}_{k+1} = \mathbf{f}^*, \quad \theta_{k+1} = \theta^* \tag{28}$$

and iterate until convergence is achieved, which is given by,

$$\|[\mathbf{f}_{k+1}, \theta_{k+1}, \phi_{k+1}]^\top - [\mathbf{f}_k, \theta_k, \phi_k]^\top\|_2 \le 10^{-6}.$$

The initial point is chosen such that it satisfies the equality constraint at $\theta = 0$:

$$\theta_0 = 0, \ \mathbf{f}_0 = \mathcal{M}^\top(\mathcal{M}\mathcal{M}^\top)^{-1}\mathbf{u}(0, 0, \epsilon, \gamma, \mathbf{N}_j). \tag{29}$$

To compute the maximum feasible pitch angle θ it is required to satisfy the constraints given in (16) and (21) for all configurations defined in (22) with $\phi = \theta$. This is achieved by solving the SCA-based optimization problem described in (25) for all $\mathbf{v}_q$, with $q \in \{1,2,3,4\}$ as defined in (27), using the same update rule and initialization given in (28), and (29), respectively.

Let the sequence $\{\theta_k\}$ converge to ${}^q\theta_j^{\max}$, for $q = 1, \ldots, 4$ and $j = 1, \ldots, 8$, where each ${}^q\theta_j^{\max}$ corresponds to a value of $\mathbf{v}_q$ in (27) and a value of $\mathbf{N}_j$ in (18). The maximum feasible roll and pitch angles, denoted by $\phi^{\max}$ and $\theta^{\max}$, must be valid for all points in (22) with $\phi = \theta$ and for all values of $\mathbf{N}_j$ in (18). Thus, $\phi^{\max}$ and $\theta^{\max}$ are computed as:

$$\phi^{\max} = \theta^{\max} = \min_{q=1,\ldots,4} \ \min_{j=1,\ldots,8} {}^q\theta_j^{\max}. \tag{30}$$

Using Lemma 1, the points $[n\pi \pm \phi^{\max}, n\pi \pm \theta^{\max}]$, for all $n \in \mathbb{N}$, satisfy the constraints given in (16) and (21).

IEEE Transactions on Automation Science and Engineering (T-ASE) paper, presented at ICRA 2026, Vienna, Austria.

The convergence of the sequence $\{\theta_k\}$, generated by the SCA algorithm, to the corresponding optimal values is established using the following Lemmas and Theorems.

Given the parameters of the tilt-rotor quadrotor in Table I and setting $\epsilon = \gamma = 1$, these results ensure that the ${}^q\theta_j^{\max}$ are indeed locally optimal solutions of the original non-convex optimization problem defined in (24), for each configuration specified in (22) with $\phi = \theta$.

Lemma 2: The following inequalities hold for $\theta, \theta_k \in \left[-\frac{\pi}{2}, \frac{\pi}{2}\right]$, with u as defined in (20) and $\hat{\mathbf{u}}$ defined in (26):

$$|\mathbf{u}(\theta, \theta, \epsilon, \gamma, \mathbf{N}_j)| \leq |{}^1\hat{\mathbf{u}}(\theta, \epsilon, \gamma, \mathbf{N}_j)|, \quad \forall j \in \{1, 2, \ldots, 8\} \tag{31}$$

where $|.|$ is component wise absolute value.

Proof: Let $\mathbf{u} := [u_1, u_2, u_3, u_4, u_5, u_6]^\top$ and ${}^1\hat{\mathbf{u}} := [\hat{u}_1, \hat{u}_2, \hat{u}_3, \hat{u}_4, \hat{u}_5, \hat{u}_6]^\top$. The function $-\sin(\theta)$ is convex and negative in $\theta, \theta_k \in \left[0, \frac{\pi}{2}\right]$. Hence, by the definition of convexity,

$$-\sin(\theta) \geq -\sin(\theta_k) - \cos(\theta_k)(\theta - \theta_k) \tag{32}$$

Using (20) with $\phi = \theta$, using (26) and (32), we get $0 \geq u_1 \geq \hat{u}_1$ for $\theta, \theta_k \in \left[0, \frac{\pi}{2}\right]$. Hence, $|\hat{u}_1| \geq |u_1|$. Similarly $-\sin(\theta)$ is concave and positive in $\theta, \theta_k \in \left[-\frac{\pi}{2}, 0\right]$. Hence, by the definition of concave,

$$-\sin(\theta) \leq -\sin(\theta_k) - \cos(\theta_k)(\theta - \theta_k) \implies 0 \leq u_1 \leq \hat{u}_1. \tag{33}$$

Hence, $|\hat{u}_1| \geq |u_1|$. Similarly, the function $\cos(\theta)\sin(\theta)$ is concave and positive in $\theta, \theta_k \in \left[0, \frac{\pi}{2}\right]$. Thus, $\hat{u}_2 \geq u_2 \geq 0$. Hence, $|\hat{u}_2| \geq |u_2|$. The function $\cos(\theta)\sin(\theta)$ is convex and negative in $\theta, \theta_k \in \left[\frac{-\pi}{2}, 0\right]$. Thus, $\hat{u}_2 \leq u_2 \leq 0$. Hence, $|\hat{u}_2| \geq |u_2|$. The function $\cos^2(\theta)$ is concave and positive in $\theta, \theta_k \in \left[\frac{-\pi}{2}, \frac{\pi}{2}\right]$. Thus, $\hat{u}_3 \geq u_3 \geq 0$. Hence, $|\hat{u}_3| \geq |u_3|$.

From (20) and (26), $u_4 = \hat{u}_4$, $u_5 = \hat{u}_5$, and $u_6 = \hat{u}_6$.

In summary, for $\theta, \theta_k \in \left[-\frac{\pi}{2}, \frac{\pi}{2}\right]$, the magnitude of ${}^1\hat{\mathbf{u}}$ is greater than or equal magnitude to that of $\mathbf{u}$ when $\phi = \theta$.□

Lemma 3: For $\mathbf{u}$ as defined in (20) and ${}^1\hat{\mathbf{u}}$ defined in (26), Consider the constraints:

$$\begin{aligned} \mathcal{M}\hat{\mathbf{f}} &= {}^1\hat{\mathbf{u}}(\theta, \epsilon, \gamma, \mathbf{N}_j), \quad \forall j \in \{1, 2, \ldots, 8\}, \\ \|[\hat{f}_{v,i}, \hat{f}_{h,i}]\|_2^2 &\leq \frac{m^2 g^2}{4}, \quad \forall i \in \{1, 2, 3, 4\}. \end{aligned} \tag{34}$$

$$\begin{aligned} \mathcal{M}\mathbf{f} &= \mathbf{u}(\theta, \theta, \epsilon, \gamma, \mathbf{N}_j), \quad \forall j \in \{1, 2, \ldots, 8\}, \\ \|[f_{v,i}, f_{h,i}]\|_2^2 &\leq \frac{m^2 g^2}{4}, \quad \forall i \in \{1, 2, 3, 4\}. \end{aligned} \tag{35}$$

where $\hat{\mathbf{f}} = [\hat{f}_{h,1}, \hat{f}_{v,1}, \hat{f}_{h,2}, \hat{f}_{v,2}, \hat{f}_{h,3}, \hat{f}_{v,3}, \hat{f}_{h,4}, \hat{f}_{v,4}]^\top$. Suppose there exists a $\theta = \theta_b$ for which the thrust constraint in (35) is violated. Then, it follows that the same $\theta = \theta_b$ also violates the constraint in (34).

Proof: From Lemma 2, the vectors $\mathbf{u}$ and ${}^1\hat{\mathbf{u}}$ have the same sign in each component. Hence, $\mathbf{u}$ can be expressed in terms of ${}^1\hat{\mathbf{u}}$ as

$$\mathbf{u} = \mathcal{T}\,{}^1\hat{\mathbf{u}}, \tag{36}$$

where $\mathcal{T} = \text{diag}([m_1, m_2, m_3, 1, 1, 1])$ with $0 < m_i \leq 1$ for $i = 1, 2, 3$. Substituting equations (34) and (35) into (36), and noting that $\mathcal{M}$ is full-rank, we obtain

$$\mathcal{M}\mathbf{f} = \mathcal{T}\mathcal{M}\hat{\mathbf{f}} \Rightarrow \mathbf{f} = \mathcal{M}^{\#}\mathcal{T}\mathcal{M}\hat{\mathbf{f}}, \tag{37}$$

where $\mathcal{M}^{\#}$ is the Moore–Penrose pseudoinverse of $\mathcal{M}$. Let $\mathcal{B} := \mathcal{M}^{\#}\mathcal{T}\mathcal{M}$. Using the singular value decomposition (SVD) of $\mathcal{M}$, we can write:

$$\mathcal{B} = \mathcal{V}^\top \mathcal{D}^{\#} \mathcal{U} \mathcal{T} \mathcal{U}^\top \mathcal{D} \mathcal{V}, \tag{38}$$

where $\mathcal{U}$ and $\mathcal{V}$ are unitary matrices, $\mathcal{D} \in \mathbb{R}^{6\times 8}$ is a diagonal matrix, and $\mathcal{D}^{\#} \in \mathbb{R}^{8\times 6}$ is its pseudoinverse. Let $\mathcal{P} := \mathcal{U}\mathcal{T}\mathcal{U}^\top$. Then $\mathcal{D}$ can be partitioned as:

$$\mathcal{D} = [\mathcal{D}_1 \quad \mathcal{O}], \quad \mathcal{D}_1 \in \mathbb{R}^{6\times 6}, \quad \mathcal{O} \in \mathbb{R}^{6\times 2},$$

where $\mathcal{D}_1$ is invertible diagonal matrix and $\mathcal{O}$ is a zero matrix. Then, we compute

$$\mathcal{D}^{\#}\mathcal{P}\mathcal{D} = \begin{bmatrix} \mathcal{D}_1^{-1}\mathcal{P}\mathcal{D}_1 & \mathcal{O} \\ \mathcal{O}^\top & \mathcal{O}_1 \end{bmatrix}, \tag{39}$$

where $\mathcal{O}_1 \in \mathbb{R}^{2\times 2}$ is a zero matrix. Using (38), (39), and the properties of similarity transform, the eigenvalues of $\mathcal{B}$ are

$$\text{eig}(\mathcal{B}) = \{m_1, m_2, m_3, 1, 1, 1, 0, 0\}.$$

From (37), the 2-norm of $\mathbf{f}$ is bounded by:

$$\lambda_{\min}(\mathcal{B})\|\hat{\mathbf{f}}\|_2 \leq \|\mathbf{f}\|_2 \leq \lambda_{\max}(\mathcal{B})\|\hat{\mathbf{f}}\|_2, \tag{40}$$

From (35), $\|\mathbf{f}\|_2 \leq 2\,mg$. If there exists a $\theta = \theta_b$ such that $\|\mathbf{f}\|_2 > 2\,mg$, then by (40), we also have $\|\hat{\mathbf{f}}\|_2 > 2\,mg$, implying that $\theta = \theta_b$ also violates (34). □

Corollary 1: From Lemma 3, equivalently (contrapositive), if θ satisfies the constraint (34), then it also satisfies the original constraint (35).

Theorem 1: Let θ_k denote the solution obtained at iteration k using the SCA technique defined in (25). Then, the sequence $\{\theta_k\}$ converges to a ${}^1\theta_j^{\max}$ such that

$$\lim_{k\to\infty} \theta_k = {}^1\theta_j^{\max} \tag{41}$$

Proof: Using Corollary 1, the solution obtained from (25) also satisfies the constraints in (35). Hence, from (26) θ_k is a feasible point of the optimization problem defined in (25).

Moreover, the optimal solution θ^* at each iteration $k \in \mathbb{N}$ satisfies $\theta_k \leq \theta^*$, which leads to

$$\theta_k \leq \theta_{k+1} \leq {}^1\theta_j^{\max} \leq \frac{\pi}{2}, \quad \forall k \in \mathbb{N}. \tag{42}$$

Therefore, the sequence $\{\theta_k\}$ is non-decreasing. Consider the candidate Lyapunov function

$$V_k = \left({}^1\theta_j^{\max} - \theta_k\right)^2, \tag{43}$$

which is positive definite for all $\theta_k \neq {}^1\theta_j^{\max}$. The difference $V_{k+1} - V_k$ is computed as

$$\begin{aligned} V_{k+1} - V_k &= \left({}^1\theta_j^{\max} - \theta_{k+1}\right)^2 - \left({}^1\theta_j^{\max} - \theta_k\right)^2 \\ &= (\theta_k - \theta_{k+1})\left(2\,{}^1\theta_j^{\max} - \theta_k - \theta_{k+1}\right). \end{aligned} \tag{44}$$

From (42), we have $\theta_{k+1} \geq \theta_k$ and $2\,{}^1\theta_j^{\max} - \theta_k - \theta_{k+1} \geq 0$. Hence,

$$V_{k+1} - V_k \leq 0, \tag{45}$$

which implies that $\{V_k\}$ is a non-increasing sequence bounded below by zero. Moreover, from (45), the condition for $V_{k+1} - V_k = 0$ is satisfied either when $\theta_{k+1} = \theta_k$, or ${}^1\theta_j^{\max} - \theta_{k+1} - \theta_k = 0$. However, since ${}^1\theta_j^{\max} \geq \theta_{k+1} \geq \theta_k$, and using (41), the only

IEEE Transactions on Automation Science and Engineering (T-ASE) paper, presented at ICRA 2026, Vienna, Austria.

possibility is $\theta_{k+1} = \theta_k = {}^1\theta_j^{\max}$. Since $V_k = ({}^1\theta_j^{\max} - \theta_k)^2$ and $V_{k+1} - V_k < 0$ and $V_{k+1} - V_k = 0$ if and only if $\theta_{k+1} = \theta_k = {}^1\theta_j^{\max}$. Hence, $\theta_k \to {}^1\theta_j^{\max}$ as $k \to \infty$. Thus, the sequence $\{\theta_k\}$ converges to ${}^1\theta_j^{\max}$. □

Theorem 2: Consider the optimization problem given in (24) and parameters given Table I with $\epsilon = \gamma = 1$. Let θ_k denote the solution obtained at iteration k using the SCA technique defined in (25). The sequence $\{\theta_k\}$ converges to ${}^1\theta_j^{\max}$. This ${}^1\theta_j^{\max}$ is a locally optimal solution to the original nonconvex problem (24) with $\phi = \theta$.

Proof: Since the optimization problem in (24) is convex, with a linear objective function, equality constraints, and convex inequality constraints, the Karush-Kuhn-Tucker (KKT) conditions can be used to characterize its optimality. The Lagrangian of the optimization problem given in (25) is

$$\mathcal{L}_1(\mathbf{f}, \theta, \mu, \nu) = C^\top \begin{bmatrix} \mathbf{f} \\ \theta \end{bmatrix} + \mu^\top \left(\mathcal{M}\mathbf{f} - {}^1\hat{\mathbf{u}}(\theta, \epsilon, \gamma, \mathbf{N}_j) \right) + \sum_{i=1}^{5} \nu_i g_i(\mathbf{f}, \theta), \tag{46}$$

where $C = [0, 0, \ldots, 0, -1]^\top \in \mathfrak{R}^9$ and $g_i(\mathbf{f}) = \left\| [f_{v,i}, f_{h,i}] \right\|_2^2 - \frac{m^2 g^2}{4}, \quad \forall i \in \{1, 2, 3, 4\}, \; g_5(\theta) = \left(\theta - \frac{\pi}{2}\right)$.

The Lagrangian corresponding to the original optimization problem (24) with $\phi = \theta$ is

$$\mathcal{L}_2(\mathbf{f}, \theta, \mu, \nu) = C^\top \begin{bmatrix} \mathbf{f} \\ \theta \end{bmatrix} + \mu^\top \left(\mathcal{M}\mathbf{f} - \mathbf{u}(\theta, \theta, \epsilon, \gamma, \mathbf{N}_j) \right) + \sum_{i=1}^{5} \nu_i g_i(\mathbf{f}, \theta). \tag{47}$$

Let $\mathbf{t} := [\mathbf{f}^\top, \theta]^\top$. The optimal solution $(\mathbf{f}_{k+1}, \theta_{k+1}, \mu_\star, \nu^\star)$ of the optimisation problem in (25) satisfies the KKT conditions. From Theorem 1, taking the limit as $k \to \infty$, we obtain

$$\theta_k \to {}^1\theta_j^{\max}, \quad \theta_{k+1} \to {}^1\theta_j^{\max}, \quad \mathbf{f}_{k+1} \to \mathbf{f}_\star.$$

At the limit, $\mathcal{L}_1(\mathbf{f}_\star, {}^1\theta_j^{\max}, \mu_\star, \nu^\star) = \mathcal{L}_2(\mathbf{f}_\star, {}^1\theta_j^{\max}, \mu_\star, \nu^\star)$. Therefore, $(\mathbf{f}_\star, {}^1\theta_j^{\max}, \mu_\star, \nu^\star)$ satisfies the KKT conditions of the original problem (24) with $\phi = \theta$, implying that it is a stationary point. To determine the nature of this stationary point, consider the Hessian of the Lagrangian:

$$\frac{\partial^2 \mathcal{L}_2}{\partial \mathbf{t}^2} = 2\,\mathrm{diag}\left(\nu_1, \nu_1, \nu_2, \nu_2, \nu_3, \nu_3, \nu_4, \nu_4, -\frac{1}{2}\mu^\top \frac{\partial^2 \mathbf{u}}{\partial \theta^2} \right). \tag{48}$$

Using `cvx`, the optimal values $(\mathbf{f}_\star, {}^1\theta_j^{\max}, \mu_\star, \nu^\star)$ of (25) are obtained for the parmeters listed in Table I, with $\epsilon = \gamma = 1$. The corresponding multiplier $\mu_\star$ is found to be $\mu_\star = [-0.1513,\ 0,\ 0,\ 0.244,\ 0,\ 0]^\top$. Furthermore, one verifies that

$$\left. \frac{\partial^2 \mathcal{L}_2}{\partial \mathbf{t}^2} \right|_{\mathbf{t} = [\mathbf{f}_\star^\top, {}^1\theta_j^{\max}]^\top, \mu_\star, \nu^\star} \geq 0, \tag{49}$$

which confirms that the stationary point is a local minimum of $\mathcal{L}_2$ with respect to $\mathbf{t}$. Because the original objective is $\min -\theta$ (equivalently, $\max \theta$), a local minimum of the Lagrangian in the decision variables $\mathbf{t}$ corresponds to a local maximum of θ. Therefore $(\mathbf{f}_\star, {}^1\theta_j^{\max})$ is a local maximiser of θ for the original optimization problem (24) with $\phi = \theta$. □

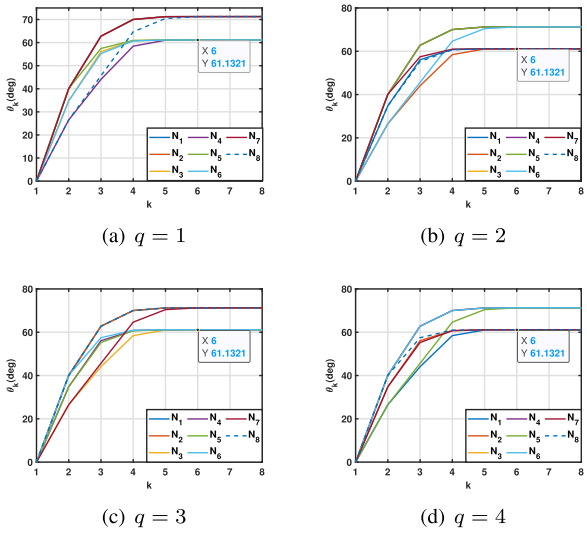

(a) $q = 1$ (b) $q = 2$ (c) $q = 3$ (d) $q = 4$

Fig. 2. Convergence of the iterative sequence θ_k using the SCA technique applied to the (25) for different configurations of $\mathbf{v}$ as defined in (27).

From Theorem 2, ${}^1\theta_j^{\max}$ is a local maximum of θ for the original non-convex optimization problem (24) with $\phi = \theta$. Following the same procedures as in Lemma 2, Lemma 3, and Theorems 1-2, and by evaluating the KKT conditions at the optimal solutions obtained from the SCA algorithm for the configurations defined in (22), together with the second-order condition (49), it follows that ${}^q\theta_j^{\max}$ is a local maximiser of θ for each configuration in (22) with $\phi = \theta$, for all $q \in \{2, 3, 4\}$.

With $\epsilon = \gamma = 1$ and the parameters given in Table I, Fig. 2 shows the sequence $\{\theta_k\}$ converges for each value of $\mathbf{N}_j$ given in (18) and each values of $\mathbf{v}$ given in (27). From Fig. 2 and using (30), the maximum value of ϕ and θ which belong to the feasible set S are given by

$$\phi^{\max} = \theta^{\max} = 61.1321^\circ. \tag{50}$$

Using Lemma 1, the points $[n\pi \pm \phi^{\max}, n\pi \pm \theta^{\max}]$, for all $n \in \mathbb{N}$, also belong to the feasible set S.

B. Minimum Thrust Required

Under the constrains of (11), the feasible ranges of ϕ and θ are restricted, as illustrated in Fig. 1. Increasing the maximum rotor thrust expands these feasible ranges. For a given rotor configuration, we seek to determine the minimum thrust-to-weight ratio χ_1 that guarantees independent control of forces and torques in all directions for any ϕ and θ. This requirement leads to the following optimisation problem

$$\begin{aligned} \underset{\mathbf{f}, \chi_1}{\text{minimize}} \;& \chi_1 \\ \text{subject to} \;& \mathcal{M}\mathbf{f} = \mathbf{u}(\phi, \theta, \epsilon, \gamma, \mathbf{N}_j), \\ & \left\| \left[f_{h,i}, f_{v,i} \right] \right\|_2 \leq \chi_1 m g, \quad \forall i \in \{1, 2, 3, 4\}, \\ & \chi_1 \geq 0. \end{aligned} \tag{51}$$

The objective of the optimisation problem given in (51) is to determine the minimum thrust-to-weight ratio required by each rotor to ensure independent control over a given set of orientations. For $\epsilon = \gamma = 1$ and the parameters provided in

IEEE Transactions on Automation Science and Engineering (T-ASE) paper, presented at ICRA 2026, Vienna, Austria.

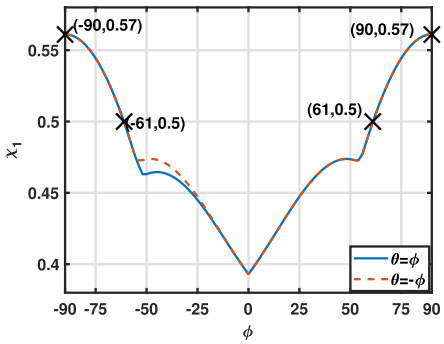

Fig. 3. Minimum thrust-to-weight ratio χ_1 for all rotors solved using (51) with $\theta = \phi$ and $\theta = -\phi$.

Table I, the boundary of the feasible set S, as shown in Fig. 1, corresponds to the condition $|\phi| = |\theta|$.

To compute the minimum required thrust-to-weight ratio, we solve the optimization problem given in (51) by setting $\theta = \phi$ and $\theta = -\phi$. Let ${}^j\chi_1^1$ denote the optimal solution of (51) with $\phi = \theta$ for each $\mathbf{N}_j$, and similarly, let ${}^j\chi_1^2$ represent the optimal solution with $\phi = -\theta$.

The minimum thrust-to-weight ratio required by each rotor must be valid for all $\mathbf{N}_j$ and both configurations $\phi = \pm\theta$. Therefore, the required thrust-to-weight ratio χ_1 is given by:

$$\chi_1 = \max_{a=1,2} \max_{j=1,\dots 8} {}^j\chi_1^a \tag{52}$$

By varying ϕ in the range $\left[-\frac{\pi}{2}, \frac{\pi}{2}\right]$ with $\theta = \phi$ and $\theta = -\phi$, the optimal thrust-to-weight ratio required in each case is computed using (51) and (52). The corresponding optimal thrust-to-weight ratios for the cases $\theta = \phi$ and $\theta = -\phi$ are shown in Fig. 3.

Using Lemma 1, the minimum required thrust-to-weight ratio across all feasible values of ϕ and θ for independent control corresponds to the maximum value of χ_1 in Fig. 3, which is 0.57. This value is dependent on the system parameters listed in Table I and the chosen values of (γ, ϵ).

Remark 2: Figure 3 shows the minimum thrust-to-weight ratio required for each rotor as a function of the maximum roll and pitch angles, ensuring that the tilt-rotor quadrotor can independently control both its position and orientation. In contrast, the work in [30] computes the minimum thrust-to-weight ratio required for the vehicle to hover at arbitrary orientations but does not establish a relationship to determine the maximum feasible roll and pitch angles for a given maximum rotor thrust. Hence, our work provides an explicit method to quantify the attitude limits for independent control of tilt-rotor quadrotor, which is not addressed in [30].

C. Effect of Disturbances on the Feasible Set S

Disturbances are inherent when operating aerial vehicles in natural environments. Among these, crosswinds are one of the most common sources of disturbance. Let, the maximum magnitudes of the disturbance force and moment are bounded by

$$\|\mathbf{d}_f\|_\infty = \|\mathbf{d}_m\|_\infty \leq D. \tag{53}$$

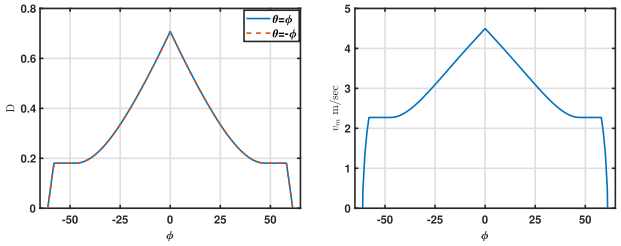

(a) D (b) v_w

Fig. 4. The maximum bound on the disturbance D and maximum wind velocity v_w as a function of ϕ (in degrees).

Given the constraint on rotor thrust (8), the objective here is to find the maximum value of disturbance bound at various orientation such that the vehicle can reject disturbance and also can independently control the position and orientation. For a given $j \in \{1, 2, \dots, 8\}$, the optimization problem can then be formulated as follows,

$$\begin{aligned} \underset{\mathbf{f}, D}{\text{maximize}} \quad & D \\ \text{subject to} \quad & \mathcal{M}\mathbf{f} = \mathbf{u}(\phi, \theta, D + \epsilon, D + \gamma, \mathbf{N}_j), \\ & \|\left[f_{v,i}, f_{h,i}\right]\|_2 \leq \frac{m\,g}{2}, \quad \forall i \in \{1, 2, 3, 4\}, \\ & D \geq 0. \end{aligned} \tag{54}$$

With $\epsilon = \gamma = 1$ and the parameters given in Table I, the boundary of the feasible set S, shown in Fig. 1, corresponds to the condition $|\phi| = |\theta|$. To compute the maximum disturbance bound, we solve the optimization problem in (54) by setting $\theta = \phi$ and $\theta = -\phi$.

Let ${}^jD^1$ denote the optimal solution of (54) with $\phi = \theta$ for each $\mathbf{N}_j$, and similarly, let ${}^jD^2$ represent the optimal solution with $\phi = -\theta$.

The maximum disturbance bound that the vehicle can reject while still maintaining independent control of its position and orientation must be valid for all $\mathbf{N}_j$ and for both configurations $\phi = \pm\theta$. Therefore, the required maximum disturbance D is given by:

$$D = \min_{b=1,2} \min_{j=1,\dots 8} {}^jD_1^b \tag{55}$$

The magnitude of wind disturbance force acting on the vehicle can be modeled using the aerodynamic drag due to wind [40], expressed as

$$\|\mathbf{d}_f\|_2 = \frac{1}{2}\rho A C_d \|\mathbf{v}_w\|_2^2$$

where $\mathbf{v}_w$ is the wind velocity in body frame $\mathcal{F}_B$. Here, ρ is the air density, A is the reference cross-sectional area of the vehicle and C_d is the drag coefficient. Thus, the maximum wind velocity v_m in any direction is given by

$$v_m = \sqrt{\frac{2D}{3\rho A C_d}} \tag{56}$$

With $\epsilon = \gamma = 1$ and the parameters given in Table I, by varying $\phi \in \left[\frac{-61\pi}{180}, \frac{61\pi}{180}\right]$ with $\theta = \phi$ and $\theta = -\phi$, the optimal disturbance bound found using (54) and maximum wind velocity given in (56) are shown in Fig. 4. This figure shows the maximum bound on the disturbance where the

IEEE Transactions on Automation Science and Engineering (T-ASE) paper, presented at ICRA 2026, Vienna, Austria.

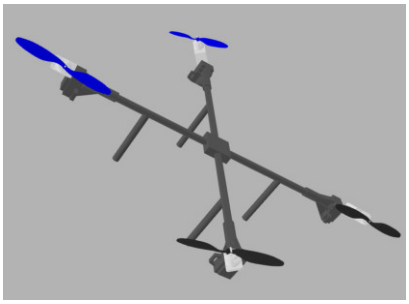

Fig. 5. Gazebo model of a tilt-rotor quadrotor.

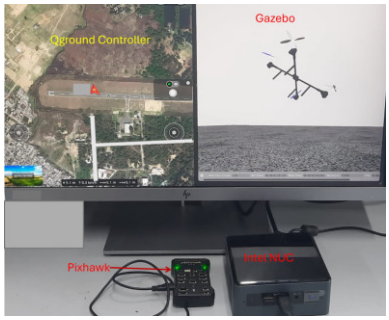

Fig. 6. PIL simulation setup for tilt-rotor quadrotor.

vehicle can be independently controlled in all directions for the maximum value of roll and pitch angles. From the figure, it can be seen that, increasing the value of D decreases the maximum value of roll and pitch angles for which independent control of force and torque is possible.

Remark 3: The feasible attitude range and the minimum thrust required by each rotor, as discussed in Section III, depend on the vehicle parameters used in this work, which are provided in Table I. For different vehicle parameters, suitable values of ϵ and γ should be chosen; however, the procedure to compute the feasible set S and the minimum thrust-to-weight ratio required remains the same as discussed in Section III.

IV. PIL Simulation Results

To validate the above results, processor-in-the-loop (PIL) simulation has been carried out in this section. For this, Pixhawk with PX4 firmware is used which supports PIL simulation [41]. The 3D model of the tilt-rotor quadrotor is developed using Gazebo [42] as shown in Fig. 5. The Gazebo simulator is run on a Intel NUC board with i5-processor. This simulator is a gateway to share data from PX4 firmware and ground station. The PIL simulation setup for tilt-rotor quadrotor is shown in Fig. 6. The controller used in this work is identical to the two-loop control scheme that is proposed in [43], which is based on quaternions. Based on the control architecture described in [43], we have implemented a two-loop control scheme for both position and attitude control. The attitude control consists of an inner loop and an outer loop: the outer loop employs a proportional controller based on quaternions, while the inner loop uses a PID controller with first order disturbance observer for angular velocity regulation.

Similarly, for position control, the outer loop is a proportional controller for position tracking, and the inner loop is a PID controller with first order disturbance observer for linear velocity control.

TABLE II
Control Parameter

Description	Value
Inner-loop PID controller for attitude	$K_p = \text{diag}(0.2, 0.2, 0.4)$ $K_i = \text{diag}(0.2, 0.2, 0.4)$ $K_d = \text{diag}(0.2, 0.2, 0.4)$
Inner-loop PID controller for position	$K_p = \text{diag}(1, 1, 1)$ $K_i = \text{diag}(0.4, 0.4, 0.4)$ $K_d = \text{diag}(0.1, 0.1, 0.1)$
Outer-loop P controller for attitude	$K_{p2} = \text{diag}(1, 1, 1)$
Outer loop P controller for position	$K_{p2} = \text{diag}(1, 1, 1)$
Disturbance observer time constant for position and attitude	$\tau_d = 1$

The control gains used for both position and attitude control are listed in Table II.

For validation of the results obtained in previous sections, two sets of simulation were performed. The first simulation is to validate the maximum roll and pitch angles for independent control. The second simulation is to verify the minimum thrust-to-weight ratio required by the each rotors such that decoupling of position and attitude is possible for all orientations.

1) Validation of Feasible Set S: In this section, the feasible set S, shown in Fig. 1 for $\phi, \theta \in \left[\frac{-\pi}{2}, \frac{\pi}{2}\right]$, is verified using PIL simulations. To validate this, the position and attitude of the tilt-rotor quadrotor must be able to track independently for all points within the feasible set. The continuous linear time varying trajectory in degrees is set as reference for the attitude which is given by,

$$\phi_d(\beta) = \theta_d(\beta) = \begin{cases} 0 & z > -2, \\ \beta t/5 & z \leq -2,\ t \leq 5 \\ \beta & z \leq -2,\ t > 5 \end{cases}, \psi_d = 0 \tag{57}$$

For the first set of simulation, β is set as 61° in (57). For the position, first tilt-rotor quadrotor moves to a desired height of 5 m from the ground, then travels along the horizontal plane to the desired point $\mathbf{p}_d = [10, 10, -5]^\top$ m. The attitude and position trajectories obtained in simulation are shown in the Figs. 7 and 8. It is observed that the vehicle can track position and attitude independently. It is also observed that the maximum shift in attitude from the reference occurs when desired position changes. The corresponding control inputs are shown in Fig. 9. As the roll and pitch angles increase, the rotor thrust and tilt angles also increase. When the roll and pitch angles reach $\frac{61\pi}{180}$ radians and the desired position changes, the thrust-to-weight ratios of F_3 and F_4 reach their maximum values. Thus, the maximum roll and pitch angles at which the tilt-rotor quadrotor can independently control its position and attitude are $\frac{61\pi}{180}$ radians.

In the second set of simulations, the objective is to validate that the tilt-rotor quadrotor cannot independently control its position and attitude when the roll and pitch angles exceed $\frac{61\pi}{180}$ radians, under the constraint of a maximum rotor thrust-to-weight ratio of 0.5. For this, β is set to $\frac{63\pi}{180}$ radians in (57). The attitude trajectory obtained from the simulation, with the maximum rotor thrust-to-weight ratio of 0.5, is shown in

IEEE Transactions on Automation Science and Engineering (T-ASE) paper, presented at ICRA 2026, Vienna, Austria.

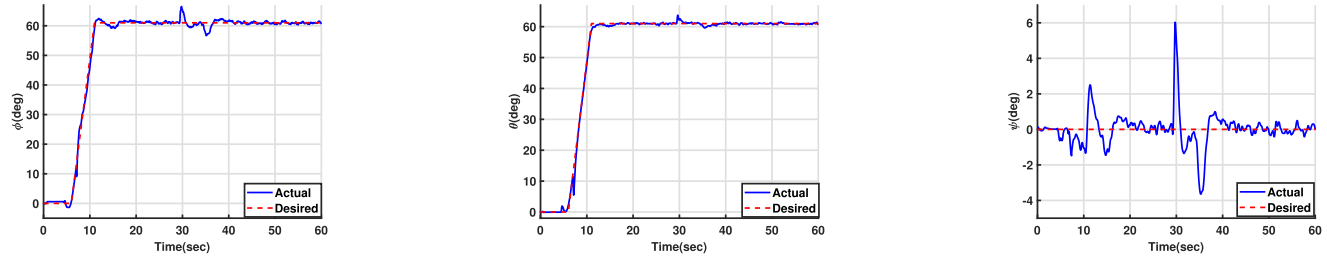

(a) roll (b) pitch (c) yaw

Fig. 7. Attitude tracking for the feasible set S.

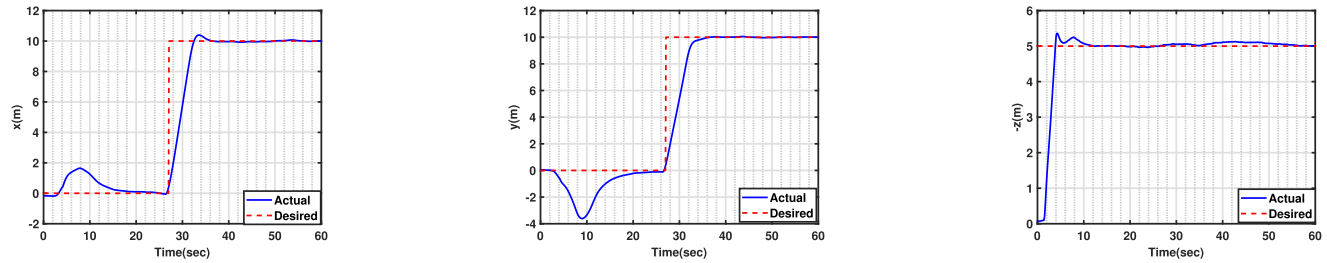

(a) x (b) y (c) z

Fig. 8. Position tracking for the feasible set S.

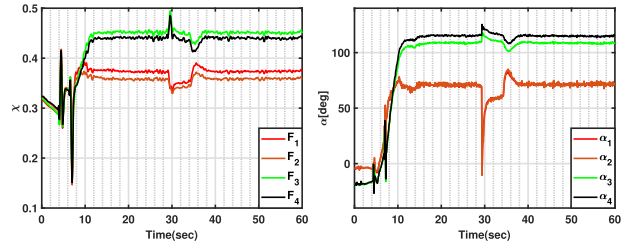

(a) Rotor Thrusts (b) Tilt angles

Fig. 9. Control input for the feasible set S.

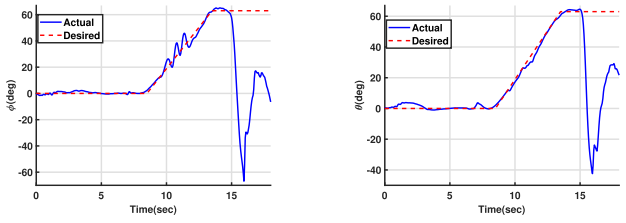

(a) roll (b) pitch

Fig. 10. Attitude tracking with the maximum rotor thrust-to-weight ratio of 0.5.

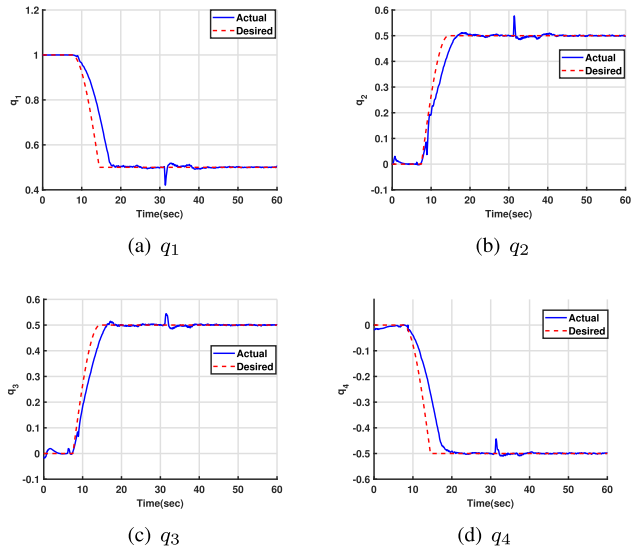

(a) q_1 (b) q_2 (c) q_3 (d) q_4

Fig. 11. Attitude tracking with the maximum rotor thrust-to-weight ratio of 0.57.

Fig. 10. It is observed that the tilt-rotor quadrotor is unable to maintain attitude control when the roll and pitch angles exceed $\frac{61\pi}{180}$ radians. Therefore, independent control of position and attitude is not possible when the roll and pitch angles surpass $\frac{61\pi}{180}$ radians.

2) Validation of Minimum Thrust-to-Weight Ratio χ_1: By increasing the thrust generated by each rotor, the maximum roll and pitch angles can be increased, enabling independent control of position and attitude. From Section III-B, the minimum thrust-to-weight ratio required to achieve independent control for all values of roll and pitch was determined to be 0.57. To verify this, the maximum angular speed of each rotor is increased by a factor of $\sqrt{\frac{0.57}{0.5}}$.

For this simulations, the reference trajectory for attitude in degrees is given in (57) with $\beta = 90°$ radians. Since the Euler angles exhibit a singularity at $\theta = \frac{\pi}{2}$, the controller used in for this set of simulations is based on quaternions. Consequently, quaternions are used to plot the results. Given the Euler angles in (57), the corresponding quaternion is given in [44].

For the position control task, the tilt-rotor quadrotor first ascends to a desired height of 5 m from the ground, then moves along the horizontal plane to the desired point $\mathbf{p}_d = [10, 10, -5]^\top$ m. The attitude and position trajectories obtained from the simulation are shown in Figs. 11 and 12. It is

IEEE Transactions on Automation Science and Engineering (T-ASE) paper, presented at ICRA 2026, Vienna, Austria.

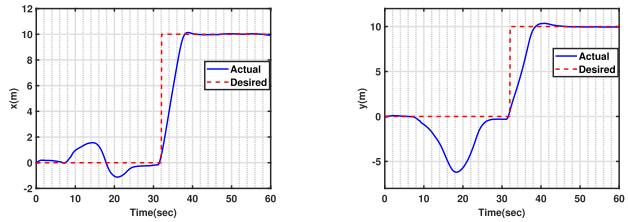

(a) x

(b) y

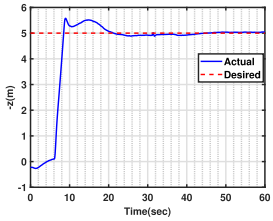

(c) z

Fig. 12. Position tracking for validation of maximum rotor thrust.

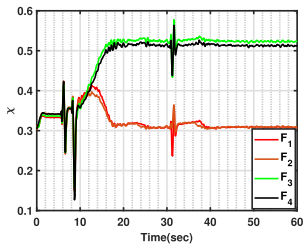

(a) Rotor Thrusts

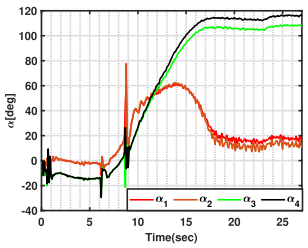

(b) Tilt angles

Fig. 13. Control input for valdiating χ_1.

observed that the vehicle is capable of independently tracking both position and attitude. Furthermore, the maximum deviation in attitude from the reference occurs when the desired position changes. The corresponding control inputs are shown in Fig. 13. As the roll and pitch angles increase, the rotor thrust and tilt angles also increase. When the roll and pitch angles reach $\frac{\pi}{2}$ radians and the desired position changes, the thrust-to-weight ratios of F_3 and F_4 reach their maximum values. Thus, by increasing the thrust-to-weight ratio of each rotor to 0.57, the vehicle can independently track its position and attitude for all possible orientations.

A. Discussion

The following observations were made from the above PIL simulations:

- The tilt-rotor quadrotor was able to independently control position and attitude with maximum roll and pitch angles of $\pm\frac{61\pi}{180}$ radians when the maximum thrust-to-weight ratio was set to 0.5 for each rotor.
- The tilt-rotor quadrotor was unable to track position and attitude for the maximum desired roll and pitch angles of $\frac{63\pi}{180}$ radians with the maximum thrust-to-weight ratio set to 0.5 for each rotor.
- When the thrust-to-weight ratio was increased to 0.57 for each rotor, the tilt-rotor quadrotor successfully controlled position and attitude independently for all roll and pitch angles.

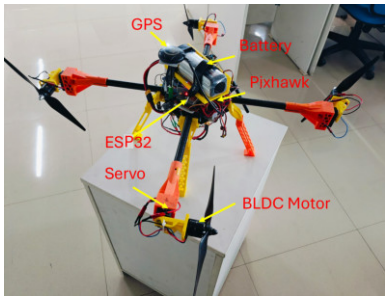

Fig. 14. Tilt-rotor quadrotor developed in-house.

In the next section, the method for determining the feasible set of an in-house built tilt-rotor quadrotor is experimentally validated.

V. Hardware Results

Figure 14 shows the tilt-rotor quadrotor developed in-house that has been used for all our experiments in this work. The main frame of the tilt-rotor quadrotor is made up of carbon fiber tubes and plates. A serial servo motor is attached to the extreme ends of the each arm. Here, Pixhawk 2.4.8 [41] is used as the autopilot board with PX4 firmware version 1.10.2. The ESP32 is used to convert control commands from the Pixhawk into the serial commands required to control the servo. A global positioning system (GPS) receiver is used for global position feedback.

The parameters for the vehicle are provided in Table I. For the developed vehicle, the maximum thrust-to-weight ratio was found to be 0.51, and the servo angles are restricted to $\pm\frac{\pi}{2}$ radians. This limitation implies that the rotors can only generate positive vertical thrust relative to the body frame. Based on these conditions, the following constraints are formulated:

$$\begin{aligned} \mathcal{M}\mathbf{f} &= {}^{c}\mathbf{u}(\phi,\theta,\epsilon,\gamma,\mathbf{N}_j), \quad \forall c \in \{1,2\}, \\ &\qquad\qquad \forall j \in \{1,\ldots,8\} \\ \|\left[f_{h,i}, f_{v,i}\right]\|_2 &\leq 0.51\ m\,g, \quad \forall i \in \{1,2,3,4\}, \\ f_{v,i} &\geq 0, \quad \forall i \in \{1,2,3,4\}, \end{aligned} \tag{58}$$

where ${}^{1}\mathbf{u}(\phi,\theta,\epsilon,\gamma,\mathbf{N}_j) = \mathbf{u}(\phi,\theta,\epsilon,\gamma,\mathbf{N}_j)$ which is given in (20) and ${}^{2}\mathbf{u}(\phi,\theta,\epsilon,\gamma,\mathbf{N}_j)$ is given by

$${}^{2}\mathbf{u}(\phi,\theta,\epsilon,\gamma,\mathbf{N}_j) = \begin{bmatrix} F_{b1} \\ F_{b2} \\ F_{b3} \\ \mathbf{M}_B \end{bmatrix} = \begin{bmatrix} -W_{b1} - \epsilon\text{sign}(W_{b1}) \\ -W_{b2} - \epsilon\text{sign}(W_{b2}) \\ -W_{b3} + \epsilon\text{sign}(W_{b3}) \\ \mathbf{N}_j(\gamma) \end{bmatrix}. \tag{59}$$

Since only vertical thrust can be generated, we need to check for two different set of ${}^{1}\mathbf{u}$ and ${}^{2}\mathbf{u}$ defined in (20) and (59) in order to satisfy the 64 distinct combination of $\mathbf{F}_b, \mathbf{M}_b$ given in (17). Similar to Lemma 1, it can be shown that if all the pairs of $[\phi,\theta] \in \left[-\frac{\pi}{2},\frac{\pi}{2}\right]$, as defined in (22), satisfy the constraints given in (58), then $[\phi,\theta]$ is the orientation for which the vehicle can independently control its position and orientation.

We use the `cvx` interface to determine whether the constraints in (58) are satisfied. The feasible set for the in-house developed tilt-rotor quadrotor is found similarly to the Algorithm 1, with the constraint specified in (58). Figure 15 shows

IEEE Transactions on Automation Science and Engineering (T-ASE) paper, presented at ICRA 2026, Vienna, Austria.

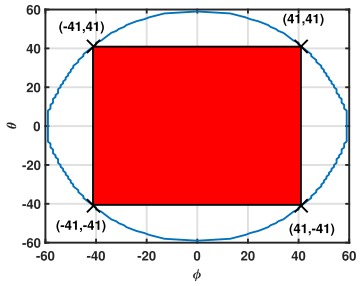

Fig. 15. Region within the blue curve for which tilt-rotor quadrotor can satisfy the constraints given in (58). ϕ and θ are independent of each other in red shaded region.

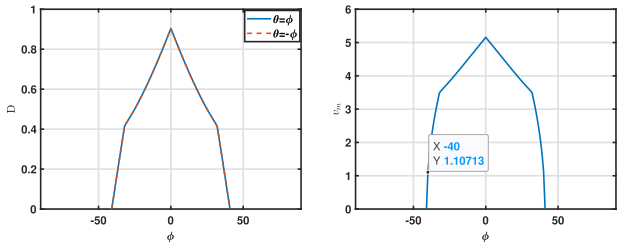

(a) D (b) v_w

Fig. 16. The maximum bound on the disturbance D and maximum wind velocity v_w as a function of ϕ (in degrees).

the maximum ranges of ϕ and θ which satisfy the constraints given in (58). The region within the blue curves in Fig. 15 shows the ranges of ϕ and θ for which the tiltrotor can independently control force and torque in all directions. The red shaded region is the maximum region for which the pitch (θ) and roll (ϕ) are independent of each other. From the figure it is observed that the maximum roll and pitch angles was found to be $\pm\frac{41\pi}{180}$ radians from the origin.

To validate the maximum roll and pitch angle limits of the in-house developed tilt-rotor quadrotor, two sets of experiments were conducted. During the experiment, the maximum roll and pitch angle was found to be $\pm\frac{40\pi}{180}$ radians for the independent control which is less than $\frac{41\pi}{180}$ radians. This deviation is due to presence of external wind. During experiment it has found that the maximum wind speed of approximately 1m/sec which correspond to disturbance bound of $D = 0.034$ (see (56)). Similar to Section III-C, the optimal disturbances obtained under the constraints in (58) for $\phi = \theta$ and $\phi = -\theta$ are shown in Fig. 16. From the figure, the maximum roll and pitch angles for a wind speed of $v_m \approx 1$ m/sec were found to be $\pm\frac{40\pi}{180}$ radians.

A. Experiment 1: Positive Roll and Pitch Angle

In this experiment, a waypoint in position and a step command for orientation are provided as references. When the vehicle reaches a safe height above the ground, a switch on the radio transmitter is triggered to set the desired attitude. The desired attitude for roll (ϕ), pitch (θ), and yaw (ψ) is set to $[40°, 40°, 0°]^\top$.

For the given task, the tilt-rotor quadrotor first ascends to a desired height of 5 m above the ground. It then travels

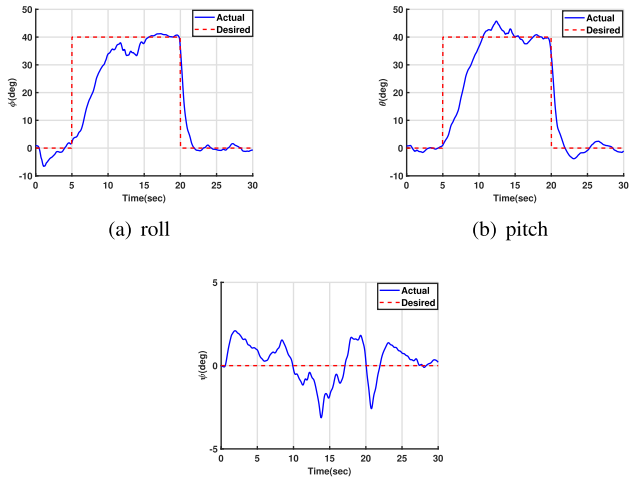

(a) roll (b) pitch

(c) yaw

Fig. 17. Attitude tracking for the maximum desired positive roll and pitch angles.

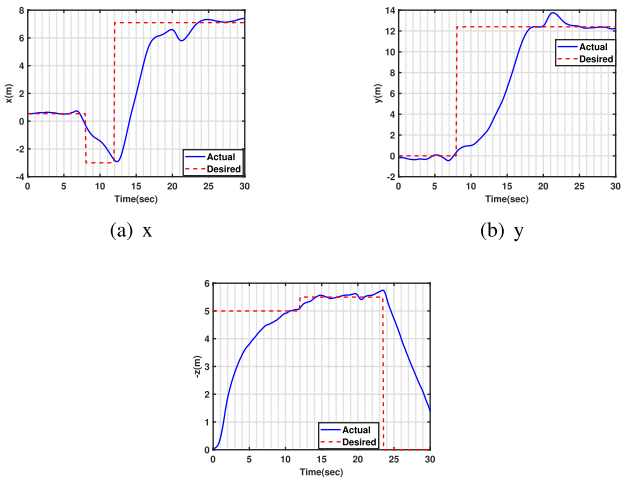

(a) x (b) y

(c) z

Fig. 18. Position tracking for the maximum desired positive roll and pitch angles.

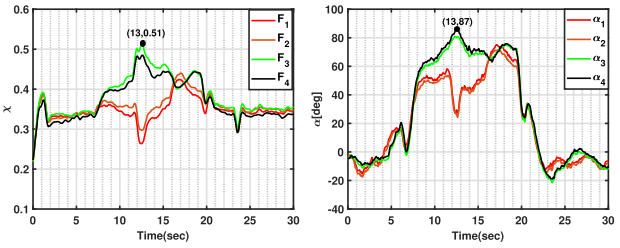

(a) Rotor Thrusts (b) Tilt angles

Fig. 19. Control input for the maximum desired positive roll and pitch angles.

sequentially to two target points, $[-2.5, 12.5, -5.0]^\top$ m and $[7.5, 12.5, -5.5]^\top$ m, before finally landing at the position $[7.5, 12.5, 0]^\top$ m. Before landing, the switch is triggered to reset the desired roll, pitch, and yaw to 0°. The attitude and position trajectories obtained from the experiments are

IEEE Transactions on Automation Science and Engineering (T-ASE) paper, presented at ICRA 2026, Vienna, Austria.

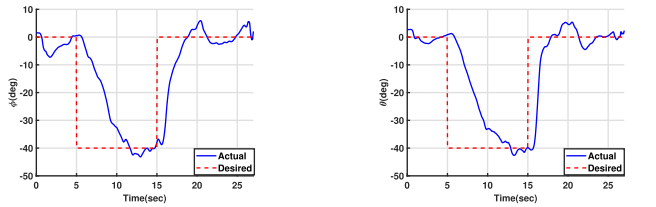

(a) roll (b) pitch (c) yaw

Fig. 20. Attitude tracking for the maximum desired negative roll and pitch angles.

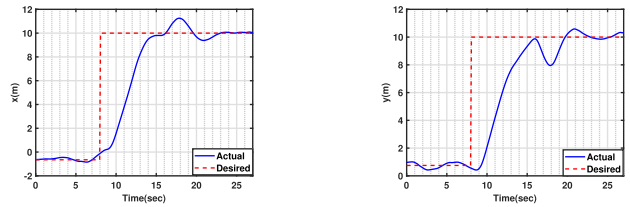

(a) x (b) y (c) z

Fig. 21. Position tracking for the maximum desired negative roll and pitch angles.

shown in Figs. 17 and 18. It is observed that the vehicle can independently track both position and attitude. The corresponding control inputs are shown in Fig. 19. As the roll and pitch angles increase the rotor thrust and the tilt angles also increase. When roll and pitch angles reaches $\frac{40\pi}{180}$ radians, and the desired position changes, the thrust-to-weight ratio of F_3 and F_4 reaches the maximum values. The next subsection validates the other extreme roll and pitch angles for the tilt-rotor quadrotor.

B. Experiment 2: Negative Roll and Pitch Angle

In this experiment, waypoints in position and a step command for orientation are provided as references. When the vehicle reaches a safe height above the ground, a switch on the radio transmitter is triggered to set the desired attitude. The desired attitude for roll (ϕ), pitch (θ), and yaw (ψ) is set to $[-40°, -40°, 0°]^\top$.

For the given task, the tilt-rotor quadrotor first ascends to a desired height of 5 m above the ground. It then travels sequentially to a target point, $[10, 10, -5.5]^\top$ m, before finally landing at the position $[10, 10, 0]^\top$ m. During landing, the switch is triggered to reset the desired roll, pitch, and yaw to 0°.

The attitude and position trajectories obtained from the experiement are shown in Figs. 20 and 21. It is observed that the vehicle can independently track both position and attitude. The corresponding control inputs are shown in Fig. 22. As the roll and pitch angles increase the rotor thrust and the tilt angles also increase. When roll and pitch angles reaches $-\frac{40\pi}{180}$ radians and the desired position changes, the thrust-to-weight ratio of F_3 and F_4 reaches the maximum values.

C. Discussion

The following observations were made from the experiments:

- Analytically, the in-house developed tilt-rotor quadrotor was expected to track position and attitude independently, with maximum roll and pitch angles of $\pm\frac{41\pi}{180}$ radians. However, experimental results showed that the maximum achievable roll and pitch angles were $\pm\frac{40\pi}{180}$ radians. This discrepancy is attributed to presence of external wind disturbance.
- Despite the presence of unmodeled dynamics, the tilt-rotor quadrotor successfully tracked position and attitude independently, maintaining stability within the observed maximum roll and pitch angle limits of $\pm\frac{40\pi}{180}$ radians.

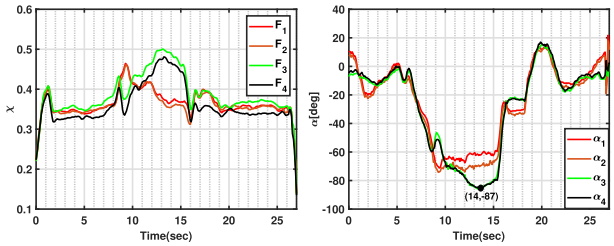

(a) Rotor Thrusts (b) Tilt angles

Fig. 22. Control input for the maximum desired negative roll and pitch angles.

A video containing the PIL simulation results and the hardware experiments discussed above can be found at: `https://youtu.be/6qjc9_KtACM`

VI. Conclusion

This paper presents the analysis of the tilt-rotor quadrotor maneuverability using convex optimization techniques. Based on the mathematical model, the feasible ranges of roll (ϕ) and pitch (θ) angles for which independent control of both position and attitude is possible were determined under actuator thrust constraints. To compute the boundary of this feasible set, a nonconvex optimization problem was formulated, capturing both thrust and moment constraints. Due to the nonconvexity of the constraints, a successive convex approximation (SCA) technique was employed to iteratively solve a sequence of convex subproblems. The convergence of the SCA iterations to

IEEE Transactions on Automation Science and Engineering (T-ASE) paper, presented at ICRA 2026, Vienna, Austria.

a local optimum of the original problem was established. It was found that, under the constraint that each rotor has a maximum thrust of $\frac{mg}{2}$, the maximum roll and pitch angles for independent control are $\pm\frac{61.1321\pi}{180}$. Additionally, a method is discussed to determine the minimum thrust-to-weight ratio required for independent control over the entire range of orientations. For the given parameters in Table I, this minimum value is found to be 0.57. The impact of bounded external disturbances such as maximum wind speed on independent control was also analyzed for independent control. It was shown that increasing disturbance bounds reduce the maximum feasible roll and pitch angles, thereby shrinking the region of independent control. Finally, the theoretical results were validated through processor-in-the-loop (PIL) simulations and real-world flight tests using an in-house developed tilt-rotor quadrotor.

REFERENCES

[1] Z. Wu et al., "$\mathcal{L}_1$ Quad: $\mathcal{L}_1$ adaptive augmentation of geometric control for agile quadrotors with performance guarantees," *IEEE Trans. Control Syst. Technol.*, vol. 33, no. 2, pp. 597–612, Mar. 2025.

[2] K. A. Kas and G. K. Johnson, "Using unmanned aerial vehicles and robotics in hazardous locations safely," *Process Saf. Prog.*, vol. 39, no. 1, p. 12066, Mar. 2020.

[3] M. Mittal, R. Mohan, W. Burgard, and A. Valada, "Vision-based autonomous UAV navigation and landing for urban search and rescue," in *Proc. Int. Symp. Robot. Res.*, 2019, pp. 575–592.

[4] H. Ding et al., "A multi-resolution approach for discovery and 3-D modeling of archaeological sites using satellite imagery and a UAV-borne camera," in *Proc. Amer. Control Conf. (ACC)*, Jul. 2016, pp. 1359–1365.

[5] K. Klausen, C. Meissen, T. I. Fossen, M. Arcak, and T. A. Johansen, "Cooperative control for multirotors transporting an unknown suspended load under environmental disturbances," *IEEE Trans. Control Syst. Technol.*, vol. 28, no. 2, pp. 653–660, Mar. 2020.

[6] S. Lee and H. Son, "Antisway control of a multirotor with cable-suspended payload," *IEEE Trans. Control Syst. Technol.*, vol. 29, no. 6, pp. 2630–2638, Nov. 2021.

[7] M. Leomanni, F. Ferrante, A. Dionigi, G. Costante, P. Valigi, and M. L. Fravolini, "Quadrotor control system design for robust monocular visual tracking," *IEEE Trans. Control Syst. Technol.*, vol. 32, no. 6, pp. 1995–2008, Nov. 2024.

[8] Z. Guo, J. Yang, S. Li, and Z. Wang, "Robust visual landing control of quadrotor on a moving platform: A sampled-data approach with delayed output and disturbances," *IEEE Trans. Control Syst. Technol.*, vol. 32, no. 6, pp. 2283–2297, Nov. 2024.

[9] A. Nguyen, D. Krupke, M. Burbage, S. Bhatnagar, S. P. Fekete, and A. T. Becker, "U sing a UAV for destructive surveys of mosquito population," in *Proc. IEEE Int. Conf. Robot. Autom. (ICRA)*, May 2018, pp. 7812–7819.

[10] W. Dong, Z. Ma, X. Sheng, and X. Zhu, "Centimeter-level aerial assembly achieved with manipulating condition inference and compliance," *IEEE/ASME Trans. Mechatronics*, vol. 27, no. 3, pp. 1660–1671, Jun. 2022.

[11] M. Tognon and A. Franchi, "Omnidirectional aerial vehicles with unidirectional thrusters: Theory, optimal design, and control," *IEEE Robot. Autom. Lett.*, vol. 3, no. 3, pp. 2277–2282, Jul. 2018.

[12] D. R. McArthur, A. B. Chowdhury, and D. J. Cappelleri, "Design of the I-BoomCopter UAV for environmental interaction," in *Proc. IEEE Int. Conf. Robot. Autom. (ICRA)*, May 2017, pp. 5209–5214.

[13] K. Bodie et al., "An omnidirectional aerial manipulation platform for contact-based inspection," in *Proc. Robot., Sci. Syst.*, Jun. 2019, pp. 1–9, doi: 10.15607/rss.2019.xv.019.

[14] S. Park and M. J. Kim, "Design of a fully actuated drone with non-isotropic wrench shape," in *Proc. IEEE/RSJ Int. Conf. Intell. Robots Syst. (IROS)*, Oct. 2024, pp. 10945–10952.

[15] M. Hamandi, F. Usai, Q. Sablé, N. Staub, M. Tognon, and A. Franchi, "Design of multirotor aerial vehicles: A taxonomy based on input allocation," *Int. J. Robot. Res.*, vol. 40, nos. 8–9, pp. 1015–1044, Aug. 2021, doi: 10.1177/02783649211025998.

[16] Y. Su, P. Yu, M. J. Gerber, L. Ruan, and T.-C. Tsao, "Fault-tolerant control of an overactuated UAV platform built on quadcopters and passive hinges," *IEEE/ASME Trans. Mechatronics*, vol. 29, no. 1, pp. 602–613, Feb. 2024.

[17] F. Şenkul and E. Altuğ, "Modeling and control of a novel tilt—Roll rotor quadrotor UAV," in *Proc. Int. Conf. Unmanned Aircr. Syst. (ICUAS)*, May 2013, pp. 1071–1076.

[18] M. Ryll, H. H. Bulthoff, and P. R. Giordano, "Modeling and control of a quadrotor UAV with tilting propellers," in *Proc. IEEE Int. Conf. Robot. Autom.*, May 2012, pp. 4606–4613.

[19] M. Ryll, H. H. Bülthoff, and P. R. Giordano, "First flight tests for a quadrotor UAV with tilting propellers," in *Proc. IEEE Int. Conf. Robot. Autom.*, May 2013, pp. 295–302.

[20] M. Ryll, H. H. Bülthoff, and P. R. Giordano, "A novel overactuated quadrotor unmanned aerial vehicle: Modeling, control, and experimental validation," *IEEE Trans. Control Syst. Technol.*, vol. 23, no. 2, pp. 540–556, Mar. 2015.

[21] D. Invernizzi, M. Giurato, P. Gattazzo, and M. Lovera, "Full pose tracking for a tilt-arm quadrotor UAV," in *Proc. IEEE Conf. Control Technol. Appl. (CCTA)*, Aug. 2018, pp. 159–164.

[22] M. Bhargavapuri, J. Patrikar, S. R. Sahoo, and M. Kothari, "A low-cost tilt-augmented quadrotor helicopter: Modeling and control," in *Proc. Int. Conf. Unmanned Aircr. Syst. (ICUAS)*, Jun. 2018, pp. 186–194.

[23] A. Oosedo, S. Abiko, S. Narasaki, A. Kuno, A. Konno, and M. Uchiyama, "Flight control systems of a quad tilt rotor unmanned aerial vehicle for a large attitude change," in *Proc. IEEE Int. Conf. Robot. Autom. (ICRA)*, May 2015, pp. 2326–2331.

[24] D. Invernizzi, M. Giurato, P. Gattazzo, and M. Lovera, "Comparison of control methods for trajectory tracking in fully actuated unmanned aerial vehicles," *IEEE Trans. Control Syst. Technol.*, vol. 29, no. 3, pp. 1147–1160, May 2021.

[25] C. Ding and L. Lu, "A tilting-rotor unmanned aerial vehicle for enhanced aerial locomotion and manipulation capabilities: Design, control, and applications," *IEEE/ASME Trans. Mechatronics*, vol. 26, no. 4, pp. 2237–2248, Aug. 2021.

[26] M. Bhargavapuri, A. K. Shastry, H. Sinha, S. R. Sahoo, and M. Kothari, "Vision-based autonomous tracking and landing of a fully-actuated rotorcraft," *Control Eng. Pract.*, vol. 89, pp. 113–129, Aug. 2019.

[27] Y. Yang, X. Yu, Z. Li, and M. V. Basin, "A new overactuated multirotor: Prototype design, dynamics modeling, and control," *IEEE Trans. Ind. Electron.*, vol. 71, no. 8, pp. 9449–9459, Aug. 2024.

[28] A. Nemati and M. Kumar, "Modeling and control of a single axis tilting quadcopter," in *Proc. Amer. Control Conf.*, Jun. 2014, pp. 3077–3082.

[29] G. Michieletto, M. Ryll, and A. Franchi, "Fundamental actuation properties of multirotors: Force–moment decoupling and fail–safe robustness," *IEEE Trans. Robot.*, vol. 34, no. 3, pp. 702–715, Jun. 2018.

[30] M. Hamandi, L. Seneviratne, and Y. Zweiri, "Static hovering realization for multirotor aerial vehicles with tiltable propellers," *J. Mech. Robot.*, vol. 16, no. 3, Mar. 2024, Art. no. 031004, doi: 10.1115/1.4056829.

[31] M. Allenspach et al., "Design and optimal control of a tiltrotor micro-aerial vehicle for efficient omnidirectional flight," *Int. J. Robot. Res.*, vol. 39, nos. 10–11, pp. 1305–1325, Sep. 2020, doi: 10.1177/0278364920943654.

[32] M. Hamandi, I. Al-Ali, L. Seneviratne, A. Franchi, and Y. Zweiri, "Full-pose trajectory tracking of overactuated multi-rotor aerial vehicles with limited actuation abilities," *IEEE Robot. Autom. Lett.*, vol. 8, no. 8, pp. 4951–4958, Aug. 2023.

[33] D. Brescianini and R. D'Andrea, "Design, modeling and control of an omni-directional aerial vehicle," in *Proc. IEEE Int. Conf. Robot. Autom. (ICRA)*, May 2016, pp. 3261–3266.

[34] H. Huang, G. M. Hoffmann, S. L. Waslander, and C. J. Tomlin, "Aerodynamics and control of autonomous quadrotor helicopters in aggressive maneuvering," in *Proc. IEEE Int. Conf. Robot. Autom.*, May 2009, pp. 3277–3282.

[35] T. Luukkonen, "Modelling and control of quadcopter," *Independ. Res. Project Appl. Math., Espoo*, vol. 22, no. 22, pp. 1–24, 2011.

[36] M. Grant and S. Boyd. (Mar. 2014). *CVX: MATLAB Software for Disciplined Convex Programming, Version 2.1*. [Online]. Available: http://cvxr.com/cvx

[37] M. Grant and S. Boyd, "Graph implementations for nonsmooth convex programs," in *Recent Advances in Learning and Control* (Lecture Notes in Control and Information Sciences). Cham, Switzerland: Springer, 2008, pp. 95–110. [Online]. Available: http://stanford.edu/~boyd/graph_dcp.html

[38] G. Ononiwu, A. Okoye, J. Onojo, and N. Onuekwusi, "Design and implementation of a real time wireless quadcopter for rescue operations," *Amer. J. Eng. Appl. Sci.*, vol. 5, pp. 1–9, Sep. 2016.

IEEE Transactions on Automation Science and Engineering (T-ASE) paper, presented at ICRA 2026, Vienna, Austria.

[39] S. Boyd and L. Vandenberghe, *Convex Optimization*. Cambridge, U.K.: Cambridge Univ. Press, 2004.
[40] A. Seth, A. James, E. Kuantama, S. Mukhopadhyay, and R. Han, "Aerodynamics and sensing analysis for efficient drone-based parcel delivery," in *Proc. 16th Int. Conf. Sens. Technol. (ICST)*, Dec. 2023, pp. 1–6.
[41] L. Meier, D. Honegger, and M. Pollefeys, "PX4: A node-based multithreaded open source robotics framework for deeply embedded platforms," in *Proc. IEEE Int. Conf. Robot. Autom. (ICRA)*, May 2015, pp. 6235–6240.
[42] N. Koenig and A. Howard, "Design and use paradigms for Gazebo, an open-source multi-robot simulator," in *Proc. IEEE/RSJ Int. Conf. Intell. Robots Syst. (IROS)*, vol. 3, Oct. 2004, pp. 2149–2154.
[43] S. Seshasayanan, S. De, and S. R. Sahoo, "Robust attitude control with fixed exponential rate of convergence and consideration of motor dynamics for tilt quadrotor using quaternions," *IEEE Trans. Autom. Sci. Eng.*, vol. 22, pp. 2445–2459, 2025.
[44] H. A. Hashim, "Special orthogonal group SO(3), Euler angles, angle-axis, rodriguez vector and unit-quaternion: Overview, mapping and challenges," 2019, *arXiv:1909.06669*.

Sathyanarayanan Seshasayanan (Member, IEEE) received the B.E. degree in electrical engineering from the SSN College of Engineering, Kalavakkam, India, in 2017, and the M.Tech. and Ph.D. degrees in electrical engineering from Indian Institute of Technology Kanpur, India. He is currently a Post-Doctoral Researcher with the Robotics and AI Team, Department of Computer Science, Electrical and Space Engineering, Luleå University of Technology, Sweden. His research interests include the control of uncrewed vehicles, space robotics, and nonlinear and robust control.

Sanjay Chaturvedi received the B.E. degree in electrical and electronics engineering from RGPV, Bhopal, India, in 2014, and the M.E. degree in digital techniques and instrumentation from SGSITS, Indore, India, in 2017. He is currently pursuing the Ph.D. degree with the Electrical Engineering Department, Indian Institute of Technology Kanpur, Kanpur, India.

Soumya Ranjan Sahoo (Senior Member, IEEE) received the B.Tech. degree in electrical engineering from the Veer Surendra Sai University of Technology, Burla, India, in 2008, and the M.Tech. and Ph.D. degrees in systems and control engineering from Indian Institute of Technology Bombay, India, in 2013. He is currently with the Faculty of Electrical Engineering, Indian Institute of Technology Kanpur, India. His research interests include the control of uncrewed vehicles, multi-agent systems, and coordinated control.